BIOMEDICAL ENGINEERING MSc PROGRAM
UNIVERSITY OF CRETE
TECHNICAL UNIVERSITY OF CRETE
FOUNDATION FOR RESEARCH AND TECHNOLOGY-HELLAS

4D Printing of Bioscaffolds for Bone Tissue Engineering

Biomedical Engineering MSc Programme

Supervisor: E. Stratakis, FORTH-IESL

2nd member committee name: Balas Costas

3rd member committee name: Ranella Anthi

Alkaios Lamprakis

Department of Medicine
University of Crete

September 2022

Acknowledgements

I would like to thank my professor Dr. Manolis Stratakis for his supervision of the thesis, his faith in me and the opportunity he gave me to work in the structures of the Institute of Electronic Structure and Lasers (IESL) of the Foundation for Research and Technology - Hellas (FORTH).

I also express my warmest thanks to Dr. Evi Kavatzikidou, team leader, for the guidance, help and excellent cooperation we have had.

I express special thanks to my professor Mr. Costas Balas and dr. Anthi Ranella, who accepted the invitation to be members of the three-member evaluation committee of my thesis.

I also express special thanks to my colleagues, Lefki Haniotaki for her initial support of the project, to Christos Ntoulias and Panagiotis Daskalakis for their help in all the technical problems that existed, to Eleni Kanakousaki for the cell culturing work, to Andreas Lemonis for the software and the help on informational issues, and the entire Ultrafast Laser Micro and Nano team Processing Lab (StratakisLab) for all the help and support they gave me all this period.

I also express sincere thanks to every member of FORTH who helped me in any way.

Finally, I would like to sincerely thank my parents who have always supported and guided me so that to improve every day.

Abstract

Bone tissue engineering is an interdisciplinary biomedical field that has gained a lot of interest the last years due to many technological breakthroughs. The use of fused deposition modelling and 3d/3D printers enables the creation of complex 3d scaffolds with the help of computer assisted design. The addition of a laser source enhances the resolution of the designs by adding a very precise subtractive tool to the equation, while also adding a fourth dimension to the printed material. The resolution a 3d printer can achieve is at best about 0.1 mm. The addition of the laser source allows to reach resolutions more than ten times higher, about 0.01 mm or less, depending on the laser source. The scaffolds are mainly made from thermoplastic polymers and polylactic acid is the gold standard, due to its printing and bio-friendly properties. Using natural PLA filament in a commercial 3d printer and nanosecond pulses from a fiber laser source, we created 4d PLA scaffolds with pore size down to 50 microns, by laser ablation. Other materials used to produce 3D and 4D scaffolds were the PCL and PCL with 10% Cellulose acetate. SEM and confocal characterization showed enhanced adhesion and proliferation of various cell cultures to the 4d scaffolds, when compared to control, while the mechanotransduction profile obtained was due to the material stiffness and cellular morphology. Such printed scaffolds with controlled micro and macro-porosities could be an advanced and safer approach for treating tissue defects eg. bone. Our results indicate a promising technique that can further be used to create scaffolds by creating more complex CADs. This Thesis has been performed at the Ultrafast Laser Micro and Nano Processing Laboratory of IESL-FORTH.

Table of contents

Abbreviations

TE	Tissue Engineering
BTE	Bone Tissue Engineering
AM	Additive Manufacturing
SM	Subtractive Manufacturing
FDM	Fused deposition Modeling
FFF	Fused Filament Fabrication
3DP	3-Dimensional Printing
4DP	4-Dimensional Printing
CAD	Computer Assisted Design
PLA	Polylactic Acid
MSC	Mesenchymal Stem Cells
ECM	Extracellular Matrix
HA	Hydroxyapatite
PGA	Polyglycolic acid
PLGA	Poly lactic-glycolic acid
PCL	Polycaprolactone
SLA	Stereolithography
DLP	Digital Light Processing
SLS	Selective Laser Sintering
PBF	Powder Bed Fusion
PP	Photopolymerization
fs	femtosecond
ps	picosecond
ns	nanosecond

CHAPTER I

Introduction

Tissue engineering is an interdisciplinary biomedical field that has gained a lot of interest the last years due to many technological breakthroughs [1] – [4]. One of the most prominent new technologies is 3D printers, which allow us to create any structure from scratch [2], [5] – [10]. They offer great customizability [1],[9] [3] are easy to set up and use, but have relatively bad resolution [1] and limited selection of, usually thermoplastic, materials [2] or demand for very high temperatures in order to operate ceramic materials per say [3], [4]. In fact, the temperature is a limiting factor since we cannot incorporate biomolecules or living cells to the material before printing [3]. In order to offset for their drawbacks, a laser source is added in the equation to achieve greater resolution and extra dimensionality to our structures. Lasers are useful in tissue engineering and especially in scaffold fabrication because they can add very small, high-quality holes or complex designs on the scaffold to guide the cells. The idea behind this project is to unify a 3d printer and a laser into an all-in-one integrated system that provides next-generation scaffolds for tissue engineering.

The combination of a 3D printer and a laser is a competent choice for tissue engineering. Its strength lies in personalization. Through computer assisted design (CAD) we can create very complex structures that are impossible with other methods and laser can add another dimension in our structures while also offering micro-/nano-machining and stress gradients [6], [7]. This approach is excellent for rapid prototyping, and since tissue engineering is referred to human individuals, this is the most desired feature. Every human being is different, therefore an implant that is tailored to the individual patient in need, is the optimal medical solution. Polylactic acid (PLA) is a very easy-to-print material, has years of research and optimization and is a suitable for bone tissue engineering material as is it biocompatible, biodegradable and has great mechanical properties.

Subject of the thesis

The aim of this thesis is to analyze the basic principles of 3d printing and laser ablation and their potential conjunction to create a novel system that will be able to work as a standalone station that will offer complex scaffold structuring for any application. The hybrid system is able to offer 10 times better resolution than that of a single 3d printer device. The specific objectives include the fabrication of 4D PLA scaffolds with specific porosity, the characterization of the morphology, structure and wetting of these scaffolds, and the investigation of the behavior of various cell lines (e.g., NIH 3T3 fibroblasts, SW10 cells and mesenchymal stem cells MSCs) on them, at several time points.

Structure of the thesis

The thesis is divided into six chapters: Chapter 1 contains the introduction, subject and structure of the thesis, chapter 2 presents the theoretical background of the basic technologies related to this thesis. These include a short introduction to additive manufacturing (AM) and materials, tissue engineering (TE), the basic principles of Fused Deposition Modeling (FDM), laser ablation and light-matter interactions, 3D printers' basics and lastly, an overview of the characterization techniques used. Then, these are compared to other methods. Chapter 3 describes the most recent breakthroughs (state-of-the-art) on the field of AM, 3D printing (3DP) and 4D printing (4DP), as well as on TE. Chapter 4 presents the analysis of the experimental setup and the auxiliary software used. This is followed by the experimental methods and discussion of the results in Chapter 5. Finally, conclusions are drawn and future extensions are discussed in the 6th Chapter.

CHAPTER II

Theoretical background

This chapter introduces in detail the basic concepts dealing with tissue engineering, 3D printers, biomaterials and laser ablation as well as their applications.

2.1 Tissue engineering

Tissue engineering (TE) an interdisciplinary field that combines the aspects of engineering with life sciences in order to develop methods that will enable for the healing [8] or replacement of damaged tissue or even whole organs [9], [10] through novel materials or devices that have properties close to those of the human body. This way, the shortage of donors [11] for tissue and organs reconstructive medicine is facing, as well as more problems, are solved [12], [13]. A usual tactic employed in TE is to create an artificial extracellular matrix (ECM), called a scaffold, that will enable for the interaction of cells with the body [14]. Scaffolds must be biocompatible and are typically porous to facilitate cell growth in the matrix and/or supply nutrients to the cells. Since the idea behind TE is to help the body heal itself, biodegradation is crucial, although not mandatory. Natural and synthetic polymers have a long history in TE, due to their medical and pharmaceutical applications. Generally, the degradation of a polymer happens by hydrolysis [15], where a polymer chain splits in the presence of water. Enzymatic and oxidative degradation is also possible in the body [15]. A very common category of tissue engineering is bone tissue engineering (BTE), where stiff scaffolds are made in order to replace fractured let's say bone or cartilage until the body heals the damaged area.

2.1.1 Bone tissue engineering

Bone [16] is a complex structure of the body, consisting of various types of tissue and cells. It consists of organic and inorganic matter and it is this combination that offers bone its great mechanical properties. The former matter is mostly collagen proteins, while the latter mostly consists of calcium and phosphate ions that nucleate to hydroxyapatite (HA) crystals.

Critical role in the scaffolds created for bone tissue engineering (BTE) plays the porosity of the bone The bones in a body are almost solid on the outside (~10-30% porosity), but can be almost hollow inside due to having many very small pores (up to 90% porosity) [14], [17]. Porosity lowers the weight of the bone by a great amount, but also lowers bone strength and stiffness [16]. This may sound as a disadvantage, but porosity is necessary as we would not be able to run if our bones were completely solid, due to their weight. Nevertheless, highly porous bones are not usually subject to great mechanical stress and the pores are filled with marrow and blood vessels, making bone a highly dynamic tissue with regenerative properties.

BTE [3], [12], [13], [18]–[23] targets on mimicking this attribute by utilizing three distinct aspects: a) scaffolds, b) cells, and c) growth factors [21]. The biocompatible scaffolds have mechanical and physiochemical properties that are close to the bone's [24] and when placed in a fractured bone part, they can stimulate the attachment and proliferation of cells on them, helping the bone regenerate its tissue. Furthermore, such engineered microenvironments are offering mechanistic insights into how the extracellular matrix (ECM) and physical forces regulate stem cells, revealing how these control self-renewal, proliferation and differentiation potentials. The cells sense the ECM mechanics and spread via transcription regulator proteins. YAP/TAZ are considered as nuclear relays of mechanical signals exerted by ECM rigidity and cell shape and as master regulator of cell–ECM interaction (mechanotransduction). In the past, pure metals or alloys were used for this cause, but science advanced to polymer composites that are closely related to bone and are characterized by high biocompatibility, osteo-inductivity and osteoconductivity [25]. Polymers offer a great solution to the materials problem, as they have all the good properties for tissue engineering [26]–[30], that will be discussed later on. A variety of polymers are biocompatible, have good physiochemical and mechanical properties and their degradation rate is similar to the rate of osteogenesis [31], making the ideal for these applications. Both natural and synthetic polymers are being used, each having its own advantages and disadvantages.

Natural polymers are biocompatible and bioactive, meaning that they are welcomed by the body and enhance adhesion and proliferation of the cells. On the downside they are more difficult to process than other materials and have not as good mechanical properties. Some popular natural polymers are proteins such as silk, collagen, gelatin, myosin, and polysaccharides such as cellulose and chitin.

In the additive manufacturing world and more specifically in the fused deposition modeling applications, synthetic polymers are preferred as they offer many desired properties such as tailoring, good mechanical strength and physiochemical attributes compared to these of the bone. Synthetic polymers are also easy to produce, low-cost and have a long shelf life, but they are short on bioactivity, hence, can cause inflammations to the host. Some widely used synthetic polymers are poly-lactic acid (PLA), polyglycolic acid (PGA), poly lactic-glycolic acid (PLGA), and polycaprolactone (PCL) which has drawn a lot of attention lately [1], [14], [17], [24], [32]–[34].

2.2 Additive Manufacturing (AM)

Additive manufacturing is a group of approaches that employ computer-aided design to construct 3D physical items that are based on layer-by-layer or spatial deposition manufacturing technologies. These technologies allow for the direct manufacture of bespoke and complicated shapes/components from metals, ceramics, polymers, and composites. There are five major categories of 3D printing processes [35]: (1) extrusion-based methods, such as fused deposition modeling (FDM), also known as fused filament fabrication (FFF), (2) photopolymerization methods like stereolithography (SLA) or digital light processing (DLP), (3) particle fusion methods, i.e., selective laser sintering (SLS), (4) material jetting, and (5) binder jetting. In this project we used a customized commercial FDM 3D printer [30].

Category	Description	Material	Mechanism
FDM	Thermal extrusion of material through a nozzle	Polymers Thermoplastics ceramics	Thermal bonding
Photopolymerization	Liquid material Cured by UV	Liquid photopolymer	Chemical reaction UV
Material Jetting	Droplets of material	Liquid photopolymer	Chemical reaction
Binder jetting	Deposition of bonding agent in bind powder	Powder	Thermal or chemical reaction
Powder bed fusion	Thermal fusing of powder	Thermoplastics Polymers Ceramics	Thermal bonding

Table 2.1. AM categories and their characteristics [6].

In table 2.1, a comparison between common AM techniques is made as well as their operation principle. Fused deposition modelling (FDM) is described as the thermal extrusion of a material, usually a thermoplastic polymer, that is bonded together thermally, forming a robust final product [12]. Photopolymerization (PP) is a technique that facilitates UV light as a curing expedient of a liquid photopolymer. Material jetting is similar to FDM, but the bonding is achieved via chemical reactions or UV curing and only liquid photopolymers are used. Binder jetting works by depositing a bonding agent in a bind powder and the final product is achieved via thermal or chemical reaction. Powder bed fusion (PBF) method uses a laser or an electron beam to melt and fuse the powdered material together [36].

Category	Resolution	Advantages	Disadvantages
FDM	0.1 mm	Low cost Low waste Personalization	Quality Low accuracy and speed
Photopolymerization	0.01 mm	High accuracy Quality	High cost Post processing
Material Jetting	0.01 mm	High accuracy	Limited materials
Binder jetting	0.01 mm	Variety of materials High productivity	Post processing Not for structural parts
Powder bed fusion	0.1 mm	Complex design Variety of materials	Low speed Structural properties Cost

Table 2.2. AM categories resolutions, advantages and disadvantages [36]

In table 2.2 we observe the different resolutions in the above-mentioned methods, as well as some advantages and disadvantages of each method. FDM is a method with relatively low resolution but very low cost, low waste and is widely available on the market. Despite their high accuracy, most methods are high cost and require post processing before the final product.

Category	Positives	Negatives
AM	Complex designs Customizability Minimal waste	Strength Heat resistance
SM	Strength Smoothness	Cost Waste
Conventional	Low cost for many pieces Durability	High cost for few pieces Waste

Table 2.3. Comparison of manufacturing techniques [36], [37]

The reason we used a hybrid FDM system is that it accumulates the AM/FDM advantages and eliminates its limitations (Table 2.3) with the use of a laser source. The complete setup offers cost and time efficiency, non-toxicity, minimal waste, high accuracy and resolution through the laser, plethora of materials and complete customizability of the scaffold, tailored to each specific patient. This last part complies with the principle of precision medicine, where a different approach is used to each individual.

A figure of merit to mathematically measure the power of a method is RTM, as spatial resolution to time for manufacturing. It is equal to the inverse of the

minimum feature dimension (d) multiplier by the created volume of material (V) per unit of time (t). High RTM indicates that a technique is suitable for commercial/industrial use, as it connects quality (resolution) with quantity (time for manufacturing). FDM and laser ablation are both techniques of high RTM ratio and relatively good spatial resolution, making them a perfect pair for commercial/industrial applications.

$$RTM = \frac{Spatial\,resolution}{Time\,for\,manufacturing} \cong R \cdot P = \frac{1}{d} \cdot \frac{V}{t}$$ **Figure of Merit**

R is the best spatial resolution that can be achieved within a technology
P is the delivery rate of the material being printed or assembled, expressed as the volume, V, of material per unit of time, t
R is expressed as the inverse of the minimum feature dimension, d

R is expressed in 1/μm, P in mm^3/min and RTM in 10^{-2} m^2/min

Technique	RTM ratio (10^{-3} m^2/minute)	Minimum feature width (μm = 10^{-6} m)	Limitations
3D™ Printing	Medium (~0.1)	~300	Presence of polymeric grains and of excess solvent
Selective laser sintering	Medium to high (~1)	<400	Presence of polymeric grains; limited to non-thermolabile materials
Laser ablation	Medium to high (~1)	<400	Thermolabile materials (cells and proteins) can be damaged during scaffold fabrication
Stereolithography	Medium (~0.5)	~30–70	Use of photosensitive polymers and initiators, which may be toxic
Two-photo polymerization	Medium (~0.05)	<1	Use of photosensitive polymers and initiators, which may be toxic
Digital light processing	Medium to high (~2)	~70–100	Use of photosensitive polymers and initiators, which may be toxic
Fused deposition Modeling	Medium to high (~1)	~200	Limited use with thermolabile materials. Evident layered structure
Electrospinning	Medium (~0.1)	<1	Difficult to realize thick scaffolds

Fig. 2.1. Formula of RTM (figure of merit of a method) and RTM ratios and features for the various additive manufacturing techniques (Source: Trends Biotechnol. 2018 Apr;36(4):384-402.).

2.2.1 3D printers

A FDM 3D printer essentially works by extruding molten plastic materials through a tiny nozzle that has the capability of precise movements, specified by a computer (CAD) [36]. The most commonly used plastics are called

thermoplastics and have the desired attribute of melting at high temperatures and then coming back to their solid state when they are cooled down. Several process parameters may be adjusted from the software, in order to achieve the best results. These include nozzle and build platform temperatures, build speed, layer height, infill and cooling fan speed.

Extruders for these printers work by utilizing the temperature difference between a cold and a hot end. The cold end pulls the material off the spool. It uses a gear or roller to pull the material and a stepper motor to control the feed rate. The cold end pushes the material into the hot end, that consists of a heating chamber and a nozzle. There a liquefier melts the material and turns it into liquid. This liquid exits the narrow nozzle, forming a thin, sticky bead of plastic that adheres to the material to which it is applied. Temperature control is essential in order for this to be successful. Different nozzle types and diameters can be used, depending on the material to be printed and the application. A typical nozzle diameter for commercial use is 0,4 mm.

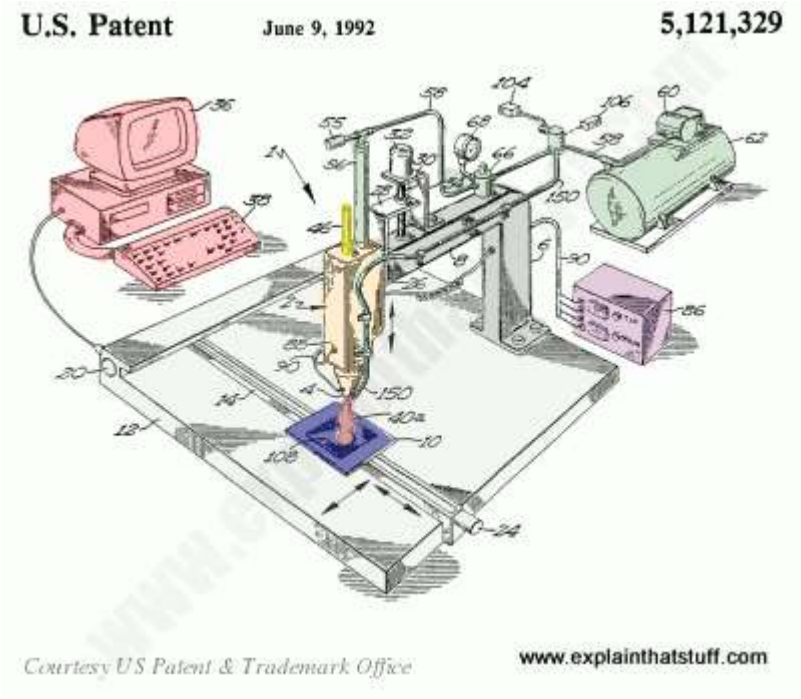

Fig. 2.2. One of the world's first 3D FDM printers, developed by Scott Crump in the 80s. In this design, the desired unit (pink, 40) is printed on a small bed (blue, 10) that moves in the horizontal axes, while the print head and nozzle (yellow, 2,4) move vertically. The setup uses compressed air from the large tank and compressor on the right (green, 62). Even though things have changed a bit, the basic principle of FDM 3D printers is still the same [38] (Fig. source: [39]).

Physics of the process

The rollers are the only drive mechanism in the material delivery system; therefore, filament is under tensile stress upstream to the roller and under compression at the downstream side acting as a plunger. Therefore, compressive stress is the driving force behind the extrusion process. The force required to extrude the material must be sufficient to overcome the pressure drop across the system, which strictly depends on the viscous properties of the melted material and the flow geometry of the liquefier and nozzle. The melted material is subjected to shear deformation during the flow. Shear thinning behavior is observed in most of the materials used in this type of 3-D printing. The temperature is regulated by heat input from electrical coil heaters.

Common defects

FDM has a lot of benefits, but they come with some clear drawbacks. While it's easy to use, mastering FDM 3D printing requires a lot of tuning and time invest. The most common print quality issues are a) warping, b) step lines, c) stringing, d) under/over extrusion etc. Most of these issues are due to mechanical mistakes, temperature fluctuations, instability, poor parameter settings (e.g. speed, temperature, flow rate) etc. While there are solutions to all of these problems, it can take multiple attempts for a high-quality outcome.

Warping

Warping (APPENDIX A.1) is the upward pulling of layers, especially of their corners, and is a common defect in 3D printers. It is caused by poor temperature control and there are many ways to limit it. One way is to monitor the temperatures of the system and reduce the temperature escape rate. Another way to prevent warping is by increasing the adhesion between the printed material and the bed and limiting thin parts and corners [40].

Layer adhesion

Layer adhesion (APPENDIX A.2) is critical for making a high end 3d-printed object. When material exits the nozzle, it has liquid form due to the high temperature and pressure. The layers bond to each other while solidifying under room temperature [45].

By optimizing several printer's parameters, aligning and calibrating the printer's bed, a high-quality final product can be produced.

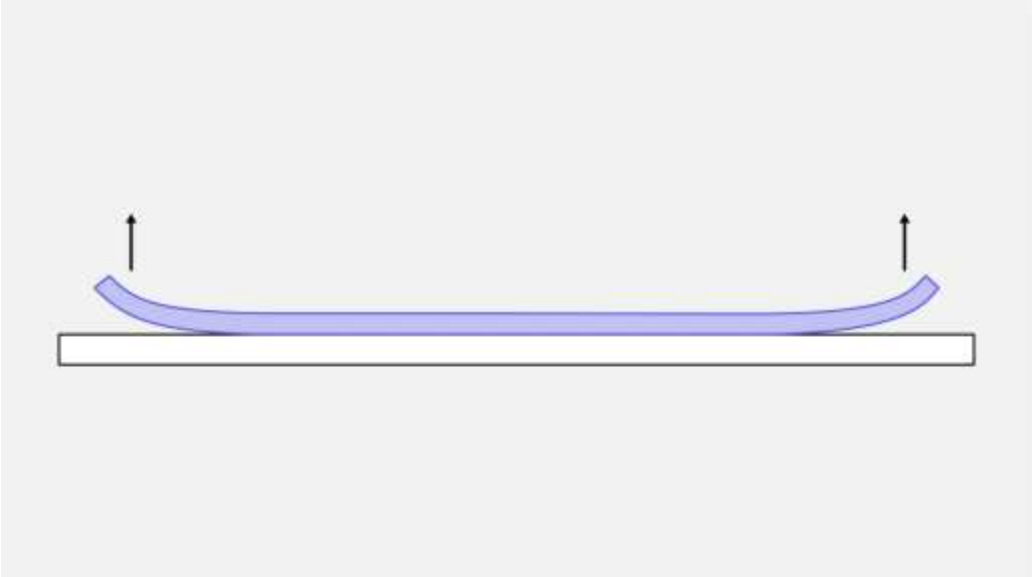

Fig. 2.3. As newly deposited layers cool, they shrink and pull the layer before them upward, resulting in warping [41].

2.3 Materials

Tissue engineering materials are obligated to be safe for the patient. The most important aspect of safety is the biocompatibility of each material used in scaffolds and implants. The notion of biocompatibility focuses on body acceptance and the lack of negative consequences after implantation. In the treatment of severe injuries and illnesses, the bioactive and biodegradable materials produced so far have been employed to accomplish the necessary function in a short period of time while also ensuring the sustainability of the surrounding tissues. Depending on the application, more properties are desirable. Since this project unifies tissue engineering with 3d printing the materials used should be printable and biocompatible.

Biodegradation, although not mandatory, is usually a wanted attribute of the scaffold. Mass loss is calculated as the ratio of initial mass (m_0) and residual mass (m_r) as follows:

$$M_L\ \% = \frac{m_0 - m_r}{m_0}\% \qquad (2.1)$$

In the present work, experiments have been carried out with various materials. We will focus on the most important ones, which, due to their properties and low cost, have already had a great impact on the field of industry and medicine.

2.3.1. Polylactic acid (PLA)

Polylactic acid (PLA) is a renewable, biodegradable polymer, made from starches. It is a non-toxic, robust, and wonderful material for 3d printing due to its physical and thermal properties that offer high-quality prints without any difficulties [34]. PLA polymers range from amorphous to highly crystalline with a glass transition temperature around 60 °C, a melting temperature around 130-180 °C, and a Young's modulus 2.7–16 GPa [42]. Several technologies such as annealing, nucleating agents' addition, composites with fibers or nano-particles, chain extending and crosslinking have been used to enhance the mechanical properties of PLA polymers. The high surface energy of PLA results in good printability, making it widely used in 3D printing.

PLA is widely used with a variety of applications in every sector of our lives. From consumer goods such as kitchenware and home appliances to medical innovations. PLA is being used as medical implant in many different forms due to its degradation into innocuous lactic acid. Depending on the exact type used, its degradation rate varies from 6 months to 2 years. This gradual degradation is desirable for a support structure, because it gradually transfers the load to the body as it heals. Thanks to its bio-compatibility and biodegradability, PLA is appealing as a polymeric scaffold for drug delivery purposes or cell adhesion and proliferation. The strength characteristics of PLA implants and scaffolds are the most investigated among all other polymers.

2.3.2. Polycaprolactone (PCL)

Polycaprolactone (PCL) is a polyester with great tissue engineering properties. Apart from its biocompatibility and biodegradability, it has good physiochemical and mechanical properties, appealing to tissue engineering applications. It is degraded by the hydrolysis of its ester bond under physiological conditions (for example, in the human body), so its use as an implantable biomaterial has received great attention. Since it degrades even more slowly than polylactide, it is of particular interest for making long-term implantable devices. Combining calcium phosphate-based ceramics and bioactive glass into PCL produces a class of hybrid biomaterials with significantly improved mechanical properties, controllable degradation rates, and enhanced biological activity, which are suitable for bone tissue engineering [43] .

PLC has a melting temperature in the range of 60-65 °C and its glass transition temperature is about -60 °C. Hence, it retains its properties under normal conditions in the body, and even at high fever or hypothermia.

2.3.3. Cellulose

Cellulose is one of the most versatile biopolymers found in nature. For more than 150 years, it has been employed as a chemical raw material [44]. Its use is now moving from sustainability-oriented development to technical solutions for a wide range of applications. New cellulose-based materials and technologies have shown promising results for real-world applications, opening up new scientific development opportunities and a new generation of sustainable and advanced materials.

Cellulose is a macromolecule that consists of both crystalline and amorphous domains. Its unique properties combined with its general availability and potential as a sustainable material have attracted considerable attention to its use in various applications. Being a natural, mechanically efficient and biocompatible material with hygroscopic properties, cellulose and its derivatives have also been recognized as useful for the formulation of hydrogels and polymer-based composites (using thermoplastic and thermoset polymers) for structural and stimulant materials fabricated by additive manufacturing.

An important form of cellulose is cellulose acetate (CA), that is highly soluble in acetone. CA based membranes are used in the separations in aqueous systems and in reverse osmosis process. It has also been used in the preparation of cellulose acetate nanofiber felt structure, cellulose acetate fibres.

2.4 Laser Ablation

2.4.1 Introduction

One way to take advantage of the benefits of nanotechnology is to process a material with a laser beam. This technique usually involves pulsed lasers, which, because of their advantages over continuous-beam wave lasers, are used to ablate part of the surface of a material to give it certain properties to it. The process is quite complicated as it involves several mechanisms and phenomena that connect light with matter. The laser penetrates the surface of the sample depending on the wavelength of the laser and the refractive index of the target material. The high electric field generated by the laser radiation excites the surface electrons and detaches them from the sample. The free electrons thus produced will collide with the atoms in the sample, resulting in an energy transfer which leads to surface heating and evaporation of the material. The fluorescence density of the laser must be greater than a critical value, called the

ablation threshold, in order to be able to extract part of the material when it strikes its surface. When the flow is high enough, the material can be transferred to the plasma state [47]. As one of the most important techniques for material processing, laser ablation can be used to drill holes with great precision, produce thin films or nanoparticles, change the surface of a material on a micro/nano scale, etc. A major advantage of the method is that it can be performed under room conditions, without any special requirements such as those of the "clean room" or vacuum chamber.

2.4.2 Lasers

Pulsed lasers (Figure 2.1) have excellent advantages over continuous lasers. The two most important parameters describing pulsed lasers are the pulse duration and the repetition rate. If, for example, the pulse is in the range of femtoseconds, thus much shorter than the time of electron-phonon interaction, which is in the order of picoseconds, then the thermal interactions are almost negligible. Moreover, with the proper focusing of the beam to a diameter of a few micrometers, we can achieve enormous intensities (TW/cm^2) and modify the refractive index of transparent materials. At laser intensities > GW/cm^2 the optical properties of the ablated material are not important as any material will absorb any wavelength at this point, due to surface breakdown and plasma formation.

2.4.3 Gaussian beams

For a Gaussian shaped beam [45], the intensity is given by the formula:

$$I(r) = I_0 e^{-(\frac{r}{w_0})^2} \quad (2.2)$$

Where w_0 is the waist (radius) of the beam's focus. For a Gaussian spatial radius (Fig. AD.1), the waist w_0 can be defined differently ways. Usually the definition is $I(w_e) = I_0/e^2$, so that $w_e=\sqrt{2}w_0$. We also use $I(w_0) = I_0/e$. The laser waist is critical for the lateral resolution of our laser induced patterns.

The radius of the laser beam at vertical distance d from the focal plane is calculated as:

$$w(d) = w_0\sqrt{1+\left(\frac{d}{d_R}\right)^2} \quad (2.3)$$

Where, d_R = Rayleigh length. The laser's focus length is defined as:

$$L = 2dR = \frac{4\pi w_0^2}{\lambda} \quad (2.4)$$

The total laser power is calculated by the formula:

$$P = 2\pi \int_0^\infty r * I(r)dr = \pi\, w_0^2 I_0 \qquad (2.5)$$

2.4.4 Laser fluence

Fluence (J/cm²) is given by (pulse energy) / (effective spot area). This should not be confused with the intensity which is equal to the (peak power) / (effective spot area) often expressed in W/cm².

For a Gaussian spatial radius (Fig. 2.1), the waist w_o (μm) can be defined differently ways. In the present work the distance is calculated with respect to $1/e^2$ of the radial flux distribution. The radial flux distribution is given by the formula [46]:

$$F(r) = F_o\, e^{-2\,(r\,/\,w_o)^2} \qquad (2.6)$$

With this definition, the ratio of maximum flux F_o and laser pulse energy

E(μJ) is defined linearly as:

$$F_o = 2E/(\pi w_o^2) \qquad (2.7)$$

At the threshold F_{th}, the square of the decomposition diameter D^2 is related to the maximum in the flow through the relationship [46]:

$$D^2 = 2w_o^2 \ln(F_o/F_{th})$$

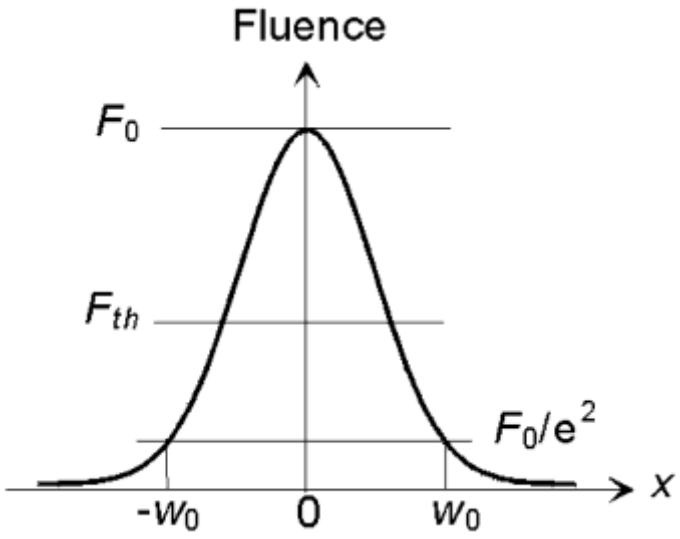

Fig. 2.4. Schematic representation of material degradation with a fixed Gaussian beam [47].

2.4.5 Number of Gaussian beam pulses

In the scanning of a line or area with a laser, we use the total number of pulses per length or per unit area [45]. One way of calculating is through the waist diameter $2w_0$. For "line scanning" at a constant speed v (mm/s) and at a pulse repetition rate f (Hz), the actual number of pulses $N_{eff,\,1Dline}$, can be set as:

$$N_{eff,\,1Dline} = 2 \cdot w_0 \cdot f / v \qquad (2.8)$$

(Meaning: number of laser pulses falling, during linear scanning, to length interval equal to the diameter $2w_0$.) For "area scanning" and distance D (step) between the scan lines, we define:

$$N_{eff,2D} = \pi \cdot N_{eff,\,1Dline} \cdot N_{eff,1Dstep} / 4 = \pi \cdot w_0^2 \cdot f / (v \cdot \delta) \qquad (2.9)$$

where $N_{eff,\,1Dstep} = 2w_0 / D$

(Meaning: number of laser pulses falling, during 2D scanning, to

an area equal to $2w_0$.)

2.5 Mechanisms of light-matter interaction

2.5.1 Main processes - Absorption mechanisms

An important quantity that interests us when we study phenomena related to light and matter is the absorption of the energy of the photons by the lattice of the material or its electrons. The absorption coefficient determines the absorption of light as a function of optical depth. However, the mechanisms by which absorption occurs depend on the nature of the material. In general, photons find the available electronic or vibrational states of matter depending on their energy. Regarding the transparent materials used in this work, the energy difference of their states is usually greater than 3 eV, which means that they do not absorb energy by photon ionization in the vis - IR spectrum, since the energy of the photons is less than the energy difference. However, in the case of intense radiation any wavelength is absorbable, thus other mechanisms can describe the interaction of light with transparent materials, such as multiphoton ionization, tunnel ionization, and avalanche ionization.

2.5.2 Multiphoton ionization

In multiphoton ionization, electrons from the valence band can absorb more than one photon at a time. The electrons go into virtual energy states and eventually into the conduction band.

2.5.3 Tunnel ionization

Tunnel ionization occurs when the intensity of the incident electromagnetic radiation is high enough to distort the dynamic energy of the atoms. The valence band electrons can then be easily excited into the conduction band.

2.5.4 Avalanche ionization

At very high intensities, the electron excitations are more than the generation of phonons, at a given time. The excited free electrons are strongly accelerated by the ionization of multiple photons or by tunneling through an electric field and then collide with atoms of the medium, ionizing them [48]. Collision-induced electrons can accelerate and ionize more atoms by triggering a chain reaction.

In some laser systems, avalanche ionization plays an essential role in optical collapse. In short, avalanche ionization of the avalanche produces macroscopic splitting of material targets, and multiphoton ionization produces seed electrons with a critical density of about 1020 cm^{-3}. These conditions force optical breakdown of the material and it becomes strongly absorbing. Even electrons with energies lower than the material's band gap may be generated [49].

2.5.5 Absorption system – Keldysh parameter

Depending on the frequency and intensity of the laser, there are three different systems involved in how a material can absorb energy through multi-photon ionization or tunnel ionization. The first system refers only to multi-photon ionization, the second system refers only to tunnel ionization and the third system concerns both multi-photon ionization and tunnel ionization.

To predict the absorption system, we use the Keldysh equation [48]:

$$\gamma = \frac{\omega}{e}\left(\frac{m*c*n*E_g*\varepsilon_0}{I}\right) \qquad (2.10)$$

where γ is the Keldysh parameter, ω is the laser frequency, I is the intensity of the focused laser beam, m is the reduced mass, e is the charge of the electron, c is the speed of light, n is the refractive index of the material, E_g is the energy gap of the material, and ε_0 is the ability of the vacuum to allow an electric field to exist. The Keldysh parameter indicates the system with which the radiation interacts with the material: if γ <1,5 we have tunnel ionization, if γ> 1,5 we have multiphoton ionization and if γ = 1,5 we have a combination of the two above [49].

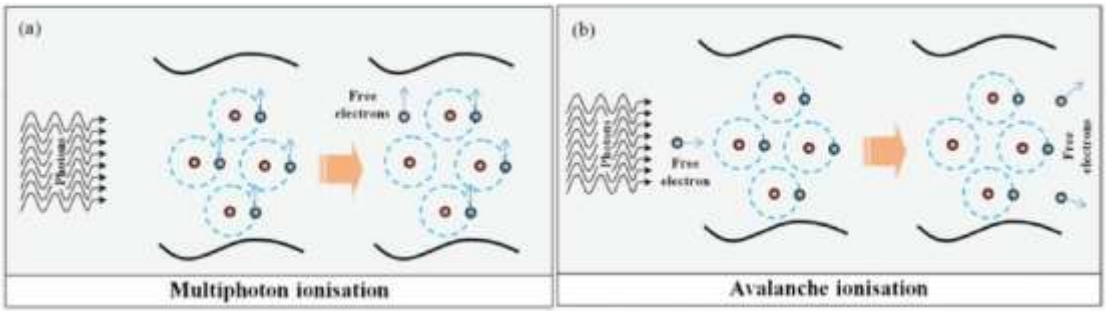

Fig. 2.5. Multiphoton ionization (a) and avalanche ionization (b) [48].

2.5.6 Secondary processes - Energy relaxation

Figure 2.3 shows the relaxation processes in chronological order. In the first processes no heat transfer takes place. In the time of femtoseconds, we have electronic discharge, which is followed by electronic cooling. Then, at a time of the order of picoseconds falls the characteristic time of the connection of the electrons with the lattice, $t_{e\text{-}l}$, which marks the end of the non-thermal interactions. At this point, heat begins to play a role, first through the out-of-equilibrium thermal melting mechanism and then through the diffusion of heat into the material lattice, causing the appearance of an unwanted level of molten material, cracks, and imperfections. In the figure, the dominance of fs pulses becomes clearer if we consider that the characteristic time (τ_L) of such a pulse is much shorter than the characteristic time for the electrons to connect to the lattice ($t_{e\text{-}l}$) and break its bonds. An ns pulse lasts much longer and reaches times when heat diffusion from the charged electrons in the lattice begins, leading to a loss of material.

In addition to the advantage of non-heat advantage, the intensity of <ps lasers is high enough and sufficient to perform nonlinear absorption processes on the target materials that cannot absorb the laser wavelength. At these high intensities, the absorption of multiple photons becomes very strong and consequently the bound electrons are released from the valence band [50]. Whe netic energy of the free electron is very high, some of the energy can be transferred to a bound electron in the target material, thus exceeding the ionization potential and creating two free electrons (Figure 2.3). This process is called (parallel) impact ionization (or avalanche) and depends to a large extent on the density of the free electrons.

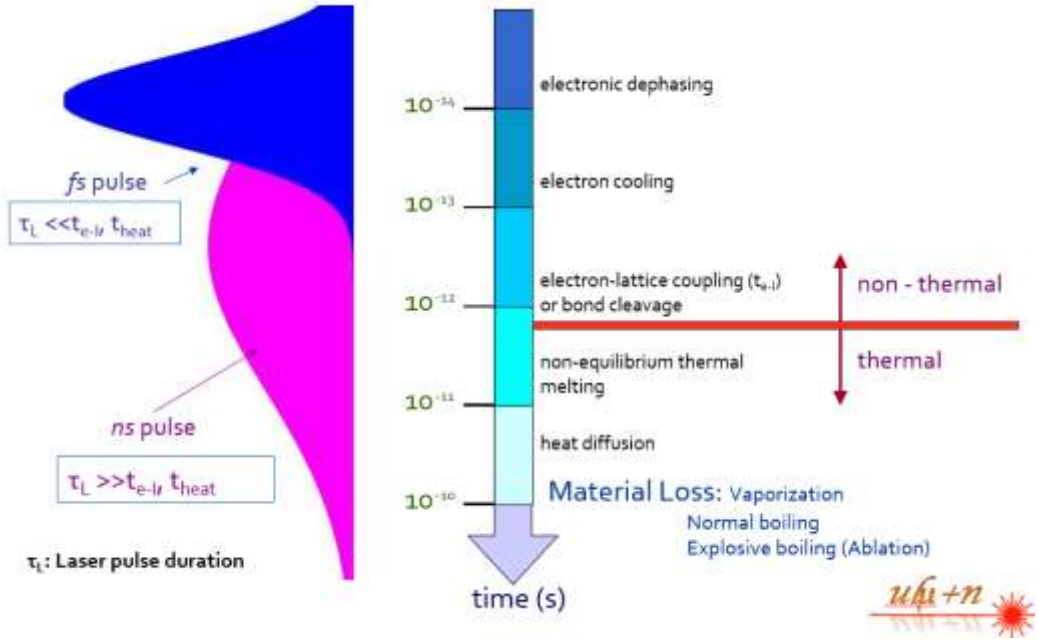

Fig. 2.6. Characteristic times of the mechanisms of interaction of light with matter. When the pulse lasts less than the time it takes for the electrons to interact with the lattice we have "cold" decomposition of the material as no heat is transferred from the charged electrons to the lattice. Otherwise, there is heat dissipation and loss of material [51].

2.6 Nanosecond pulsed laser processing

There are numerous models that describe nanosecond-laser ablation. Each model uses only one dominant mechanism to try to describe this phenomenon, but in reality, different interactions and their coupling must be analyzed.

2.6.1 Polymers

Polymers have a relatively high molecular weight. They usually consist of tens of thousands of atoms, forming molecules called monomers that repeat themselves thousands of times forming the chain we call a polymer. The molecular forces are weak (~0.5 eV) but atoms share neighboring electrons forming covalent bonds that are strong (~3-8 eV). An IR photon of about 1000 nm wavelength has energy E~2 eV as shown in fig 2.4, using the formula E(eV) =1240/λ(nm). This means that a single photon's energy is not sufficient to break the bonds photochemically. Thus, multiphoton absorption is necessary in order to break these bonds and ablate the material.

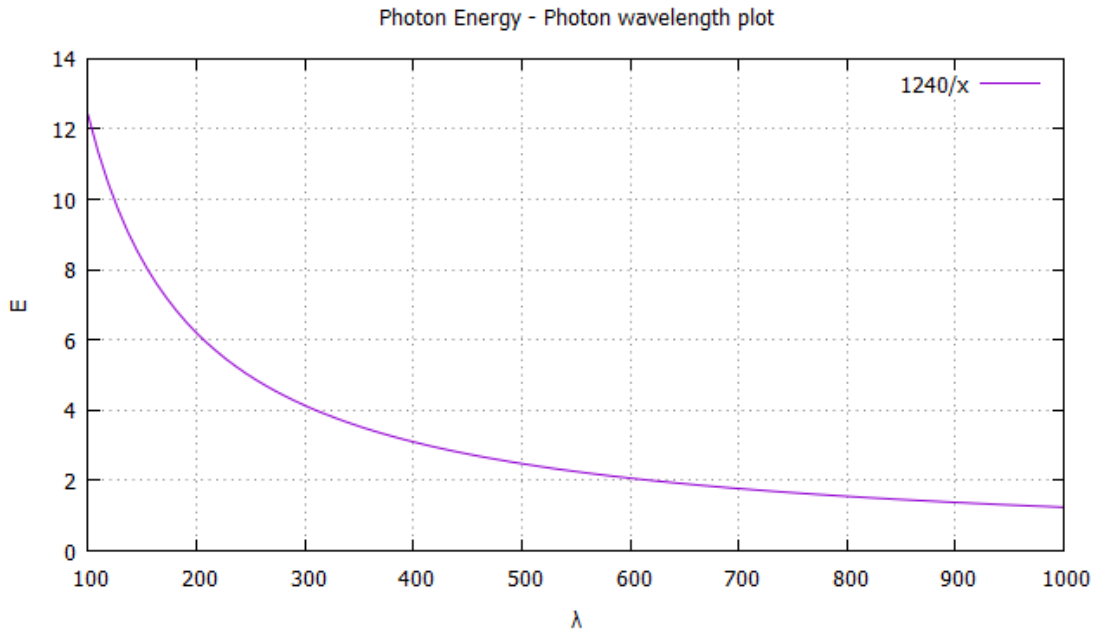

Fig 2.7 Photon energy to photon wavelength plot using the formula E(eV) =1240/λ(nm).

2.6.2 Photophysical ablation

Photophysical ablation [52] describes both thermal and non-thermal mechanisms that play role in the ablation rate. This is true when the life time of electronically excited species or broken bonds is very long so during this time species desorb from the surface before heat diffusion. This process is enhanced by the temperature rise.

2.6.3 Photochemical ablation

Another case is the direct bond breaking and desorption of surface atoms or molecules due to very high energy photons being absorbed [52]. Photochemically dissociated bonds can also build stresses that lead to mechanical ablation of the material.

2.6.4 Photothermal ablation

If the energy of the laser is instantly transformed to heat, it changes the optical properties of the material [52]. This leads to thermal ablation that comes with or without surface melting. Thermal effects can also lead to very high stresses that explosively ablate the material. Boltzmann statistics describe the immediate energy conversion to heat and Arrhenius rate equation explains the thermal bond breaking.

2.7 Characterization methods

In order to receive a great amount of information from our scaffolds we need sophisticated machinery to observe at the micro-level. Scanning electron microscopy is a typical system we use, due to its many benefits.

2.7.1 Scanning Electron Microscopy

With a scanning electron microscope (SEM), we use various properties of electrons to achieve enormous magnifications that reach into the order of millions. Unlike microscopes that use light and ordinary lenses to produce an image of an object, the SEM uses electrons and electromagnetic lenses to produce an image of an object's surface on a computer screen or television. In order to operate this instrument, it is necessary to create a sufficient vacuum by constantly pumping out air after placing the object (sample) under the microscope. For this reason, it is extremely important to keep the specimen as clean as possible during preparation. In an insufficient vacuum, the electrons collide with the air molecules and are absorbed [53].

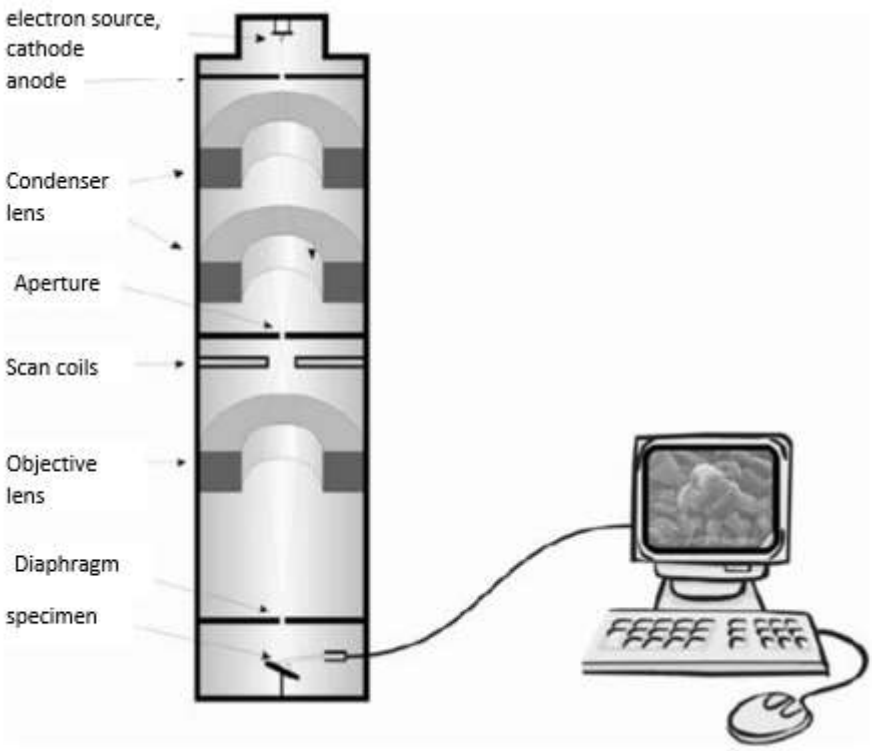

Fig. 2.8. Schematic representation of a scanning electron microscope [54].

The operation of the SEM (fig. 2.5) can be summarized as follows:

1. An electron beam is generated by a tungsten wire and scans the surface of the sample at high speed. A high voltage ascent-descent system is used for acceleration.

2. lenses focus the beam on the desired point of the sample and the electrons either penetrate the sample or scatter, simultaneously producing secondary electrons, backscattered electrons, X-rays and Auger electrons from the beam-sample interaction.

3. the backscattered electrons are reflected by elastic dispersion after hitting the sample and are usually used together with X-ray spectra.

4. the secondary electrons have relatively little energy and originate from the surface of the sample, so they give us most of the information about the surface structure.

Pretreatment is required for the observation of SEM nonconductive materials, such as the polymers used in this work. The non-conductive material should be covered with a layer of conductive material, such as gold, platinum or an alloy [54]. Otherwise, if the surface is charged during measurement, reflection of the emitted beam may occur, altering the emission of secondary electrons.

2.7.2 Sputtering

In order to observe a sample in the SEM, we utilize sputtering, a phenomenon in which a conductive solid material is bombarded by plasma and tiny particles are ejected from its surface (fig. 2.6). This way a thin layer of conductive material deposits on our specimen surface and observation in SEM is possible, since the conductive material will interact with the electrons emitted from the microscope. This is done by special devices called sputter coater. These use argon gas, metal pieces (usually gold, platinum or silver), and an electric field in order to deposit a thin conductive film on the surface of the non-conductive sample. Sputter coating prevents charging of the specimen and increases the signal to noise ratio by improving the secondary electron emission [55].

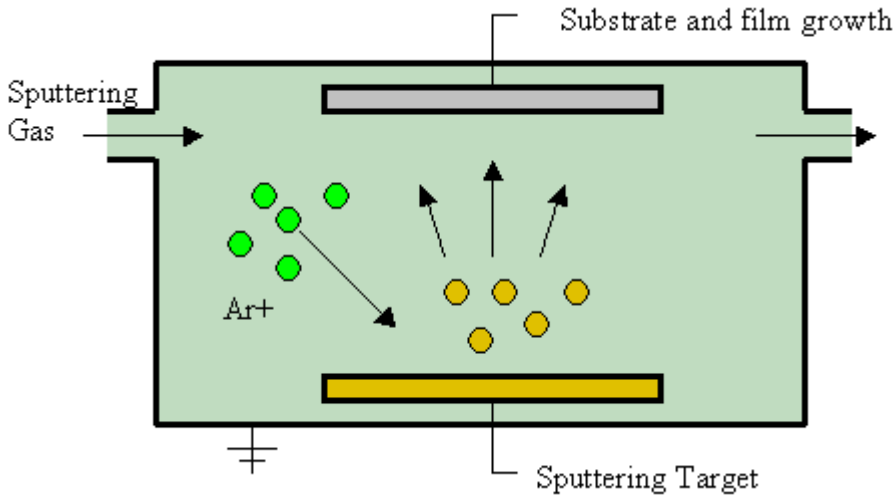

Fig. 2.9. Schematic representation of sputter deposition [56].

The sample is placed in a vacuum chamber in order to have the minimum impurities on our film from dust or air particles. In order to keep the specimen perfectly still, we use carbon tape, that prevents it from moving and cause uneven deposition, while also grounding it. Argon gas fills the chamber and the electric field causes electrons to escape from the argon atoms and make them positive ions. These ions are attracted to a negatively charged piece of gold and bombard it, causing gold atoms to eject from its surface and deposit on the sample's surface, producing a thin gold coating that is our conductive film. The film's thickness is proportional to sputtering duration [56].

An important advantage of sputter deposition is that it almost does not heat the sample and makes possible the observation of samples that would otherwise be impossible or of inferior quality. A downside is that the sputtered samples cannot be used in biomedical applications, thus we "sacrifice" the sample in order to be able to observe it.

2.7.5 Confocal Microscopy

Confocal microscopy is an optical imaging technique that uses a pinhole to block out-of-focus light, thus increasing the obtained picture's optical resolution and contrast [57]. The technique is capable of capturing 2D images, but repeating for different depths in the sample, a 3D reconstruction of the structure is possible. Typical applications of this method are in life sciences, semiconductor inspection and materials science.

The basic concept of confocal microscopy is that by limiting the area of illumination, only the fluorescence light that is produced very close to the focal plane is detected. Thus, the image's optical resolution is superior to that of wide-field microscopes. Confocal microscopes may reach resolutions of hundreds of nanometers laterally and axially [58].

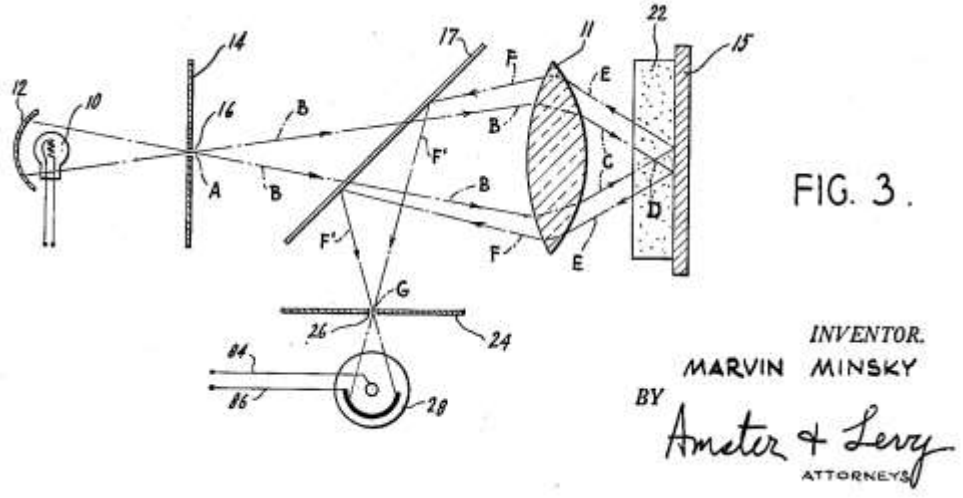

Fig. 2.10. Confocal microscope's blueprint.

CHAPTER III

State of the Art

Tissue engineering is an interdisciplinary field that combines life sciences with engineering and materials science in order to replace and heal damaged human tissues or organs. As technology advances, tissue engineering devices and materials are becoming more and more sophisticated. The basic idea is to utilize scaffolds, cells and growth factors. This combination acts as a replacement of the damaged tissue until the body heals itself or even permanently [1]–[62]. Providing a physical structure is not enough for biomedical applications, thus these materials usually mimic the ECM, providing the necessary environmental conditions for cells to attach, grow and proliferate[17], [23], [32], [61], [63]–[65].

Diloksumpan et al. offered a fresh perspective at 2020 by combining hydrogels and ceramics to create a multi-material final product (fig. 3.1) that has all the good properties of the hydrogel but also the stiffness of the ceramic offers extra protection [66]. This research studied the behavior of equine MSC cells in the scaffolds. As seen in fig. 3.2 the composite structure had no negative effect on cell survival due to detrimental degradation byproducts or uncontrolled pH changes. After several days the cells grew and proliferated, as confirmed via immunofluorescence. Overall, the samples did show osteogenic potential and regeneration.

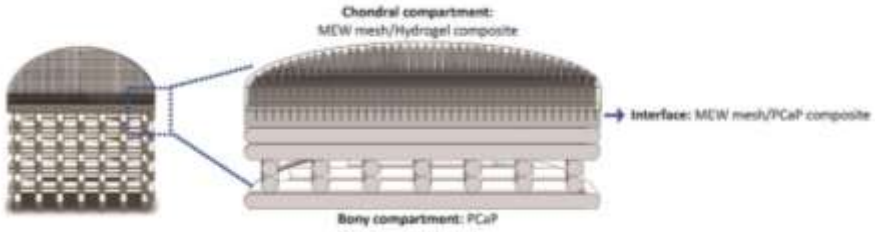

Fig. 3.1. Creation of bone-cartilage using a combination of materials.

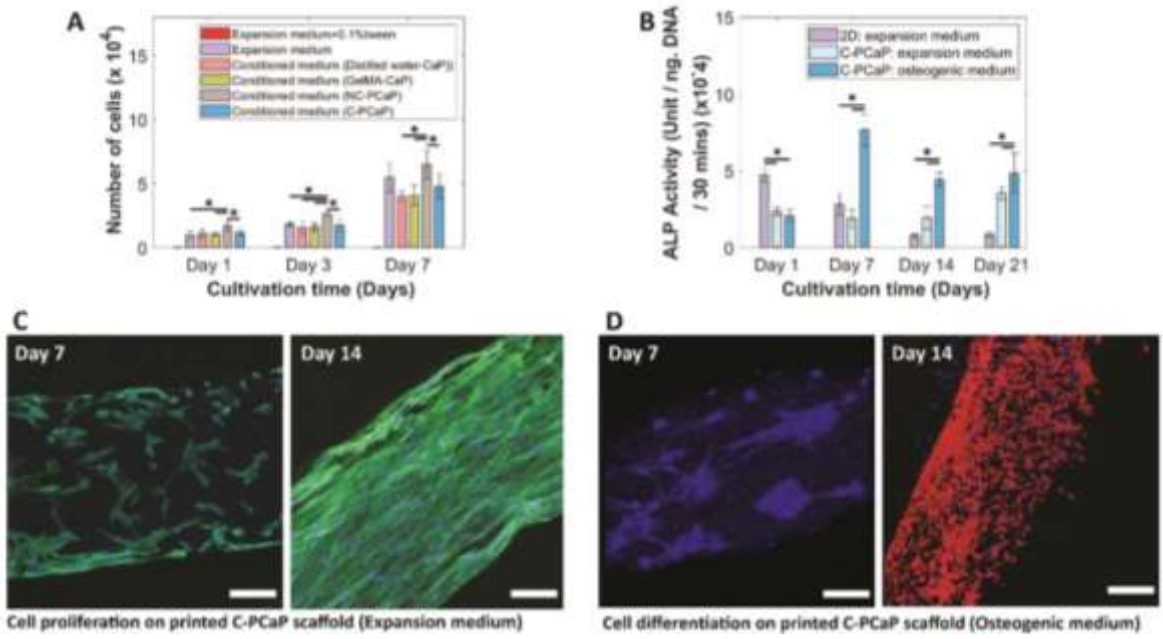

Fig. 3.2. Cytocompatibility and osteogeny in vitro. Scale bars: 100 µm.

A work done by Otto et al. in 2021 has also shown interesting results in the biofabrication of auricular structures [9]. The first observation is the expected change in mechanical strength, that depends on the strand spacings, as seen in fig. 3.3a below. The sGAG/dsDNA content also seems to relate to the porosity of the scaffold, among other things (fig. 3.3b). This way, one can choose the strand distance depending on the application the scaffolds will be used.

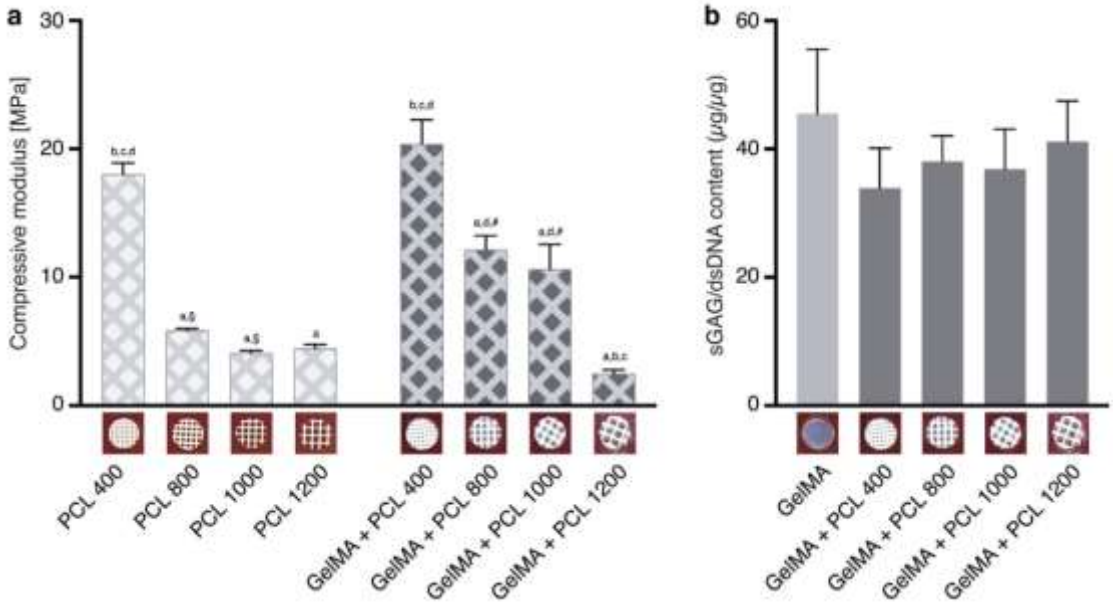

Fig. 3.3. (a) compressive modulus in respect to strand spacing and (b) sGAG/dsDNA content in respect to strand spacing.

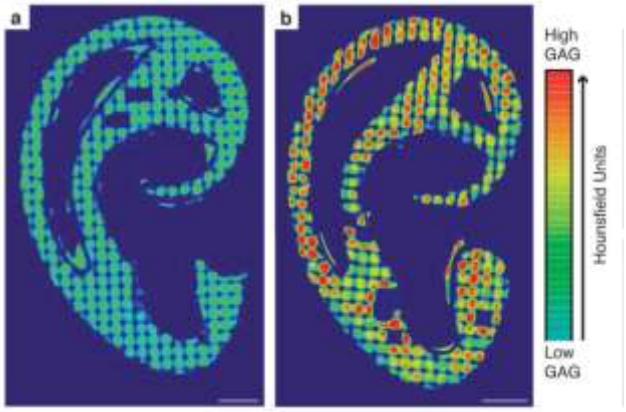

Fig. 3.5. Qualitative analysis of bio-scaffolds for (a) 1 day and (b) 30 days of culturing.

As seen in fig. 3.5, the whole scaffold filled with cells. The distribution of GAGs in the scaffolds seems to be high after 30 days of culturing (fig. 3.5b) than in day 1 (fig. 3.5a). From the figure, we can observe that the highest concentration of GAGs appears in the helix, antihelix and tragus areas.

The scaffolds presented in this study show that it is possible to create hybrid ear-shaped constructs with inherent regenerative potential, in a short time period.

As a matter of fact, healing rates and improvements in mechanical and physiochemical properties are at the center of attention. W. He et al. research (2021) on bacterial cellulose scaffolds for wound healing demonstrated superior healing rates of up to 31.8% higher than control, on a 90 days period [67]. H. El-Hamshary et al (2021) created biocompatible, biodegradable polymer fibrous matrices that provided an environment similar to ECM, resulting in faster and better wound healing, while protection from bacteria was also observed [68].

Another topic of research is the creation of hierarchical structures. Xiangjia Li et al. (2021) created bio-scaffolds using ceramics [69], with hierarchical pores and the lowest pore size was 50 microns. Table 3.1 also shows the different methods capabilities on this area.

Method	Material	Porous structure size	Porous structure shape	Porosity (%)	Mechanical strength (MPa)	Ref.
Freeze-casting	HA/TCP	40–200 μm	Uncontrollable	31.4–72.5	1.95–2.98	[5, 13]
Foam replica method	HA/TCP	500 μm	Uncontrollable	87	0.05	[6]
Solvent casting	PGA/TCP	483 μm	Uncontrollable	88.4		[14]
Particle leaching	PLA/β-TCP	300–420 μm	Uncontrollable	50	4–6	[15]
High-pressure pressing	HA	1 μm	Uncontrollable	20–40	40–100	[16]
Injection molding	HA/EVA/PA66	200–600 μm	Uncontrollable	60–75	5–10	[17]
Fused deposition modeling (FDM)	TCP	300–500 μm	Mesh matrix (Controllable)	29–44	0.24–1.44	[18]
Powder binder jetting	TCP	400–800 μm and ≤5 μm	Mesh matrix (Controllable)	27–50	3–11	[19, 20]
Vat photo-polymerization	HA	1000 μm	Mesh matrix (Controllable)	27	4.3–11.2	[21]
Extrusion-based printing	HA/TCP	50–580 μm	Mesh matrix (Controllable)	30–70	20–100	[22]
Our μMIP-SL	HA/TCP	20–1000 μm and ≤5 μm	Free-form structure (Controllable)	20–80	15	

Table 3.1. Comparison of 3d printed HA/TCP scaffolds.

The use of composites is widely preferred nowadays in the place of single materials, as there is no perfect material for TE. This way research tries to eliminate the negative aspects and enhance the positives of each material, in a chase for superior results. Babilotte J. et al. (2020) showed that the addition of nHA to PLGA (fig. 3.6) displayed a positive impact on osteo-differentiation in vitro [70].

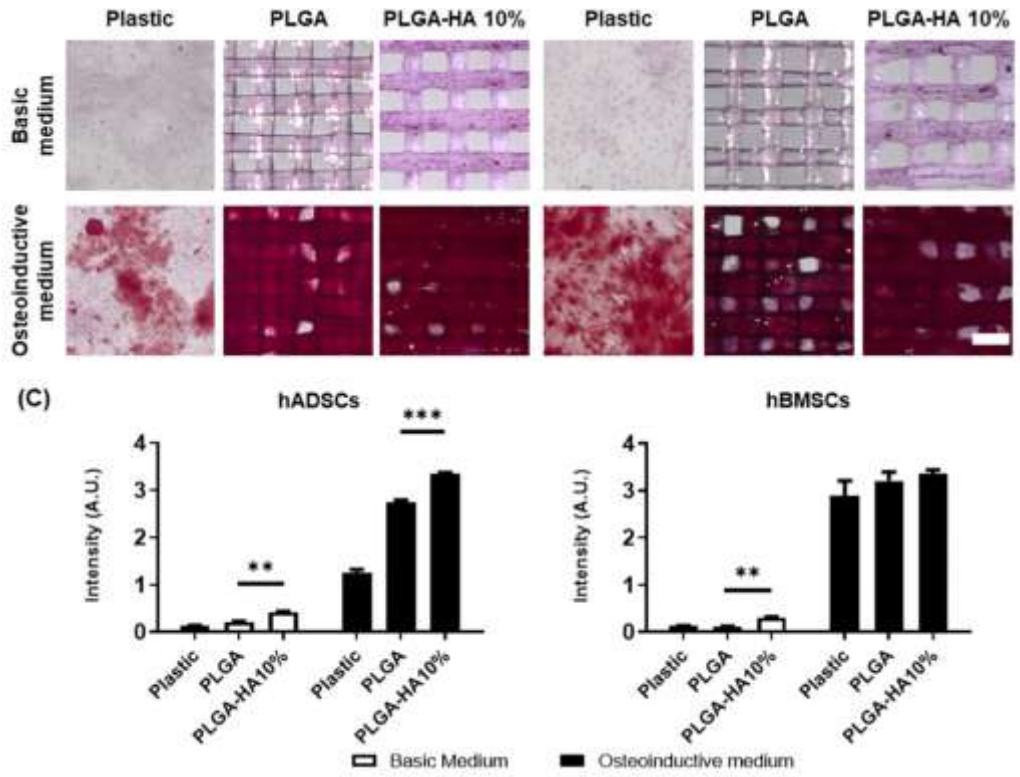

Fig 3.6. Osteo-differentiation in vitro of plastic, PLGA and PLGA-HA 10% scaffolds in basic and osteo-inductive medium.

A rise in the degradation rate was also observed at this research (fig. 3.7). This is an edifying observation, as depending on the application, different degradation rates may be favorable. Its manipulation by using just the right amount of composite materials can be very useful, as it will not alter the biological properties of the scaffold.

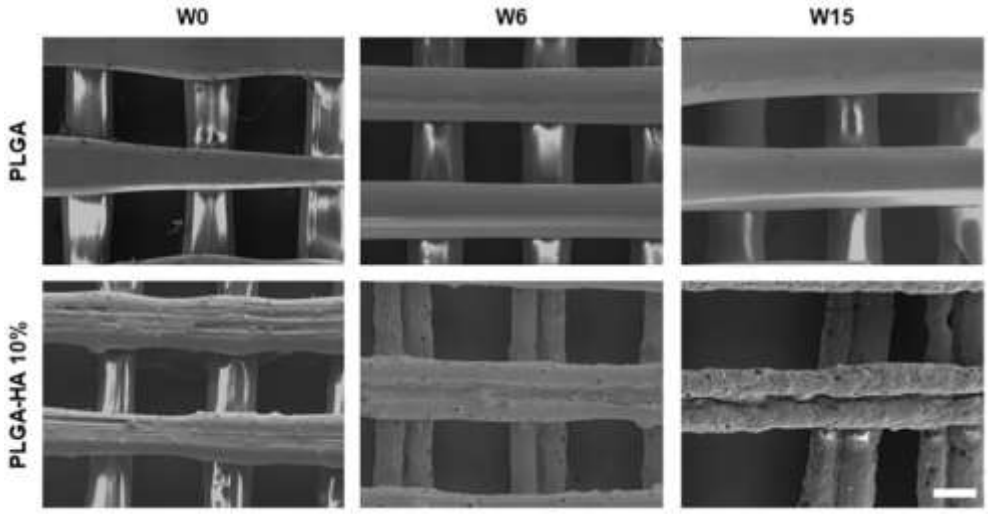

Fig. 3.7. Degradation rate of PLGA and PLGA-HA 10% for 0 to 15 weeks.

Despite the 3d printing technology having brought great advancements in the biomedical field, there is a long road to achieve the level of results needed for this kind of applications. The ECM is a very complex environment that is hard to replicate in vitro and the CAD designs are not always printed as visualized. Some great advancements using hydrogels still have not found a way to solve the malnourishment and insufficient oxygen supply of the cells in the scaffolds. Additional problems like low cell survival, proliferation or attachment exist or even bad mechanical properties in the case of several biopolymers. The human body is very complex; thus, several different approaches are made for each body part/tissue that is being replicated.

A recent effort to surpass the contemporary solutions is the research of Wang X. et al. [67] to create responsive scaffolds with biomimetic enrichment channels for bone regeneration, that utilize the microfluidics principle. Their strategy is to fabricate black phosphorus (BP) incorporated fibrous scaffolds with channels that expand or shrink in response to temperature changes, induced by near-infrared (NIR) light. This way the cellular infiltration to the channels is facilitated. The results showed that the photothermal dynamic channels favored the growth and regeneration of cells. Fig. 3.8a demonstrates how cells (green dots) enter the scaffold's channels when NIR irradiation stops and swelling starts. This is validated from their results, as seen in fig. 3.8b-e, where the results confirm that cells grow and proliferate inside the dynamic channels for up to 5 cycles of alternating NIR on/off and up to 5 days of observation. NIR-enhanced bone regeneration of a rat cranial defect model was also observed in vivo for a 2–6-week time interval. Quantitative analysis revealed that the BP incorporated and irradiated with NIR group showed the highest bone tissue volume/total tissue volume and bone mineral density, among the control and not irradiated groups.

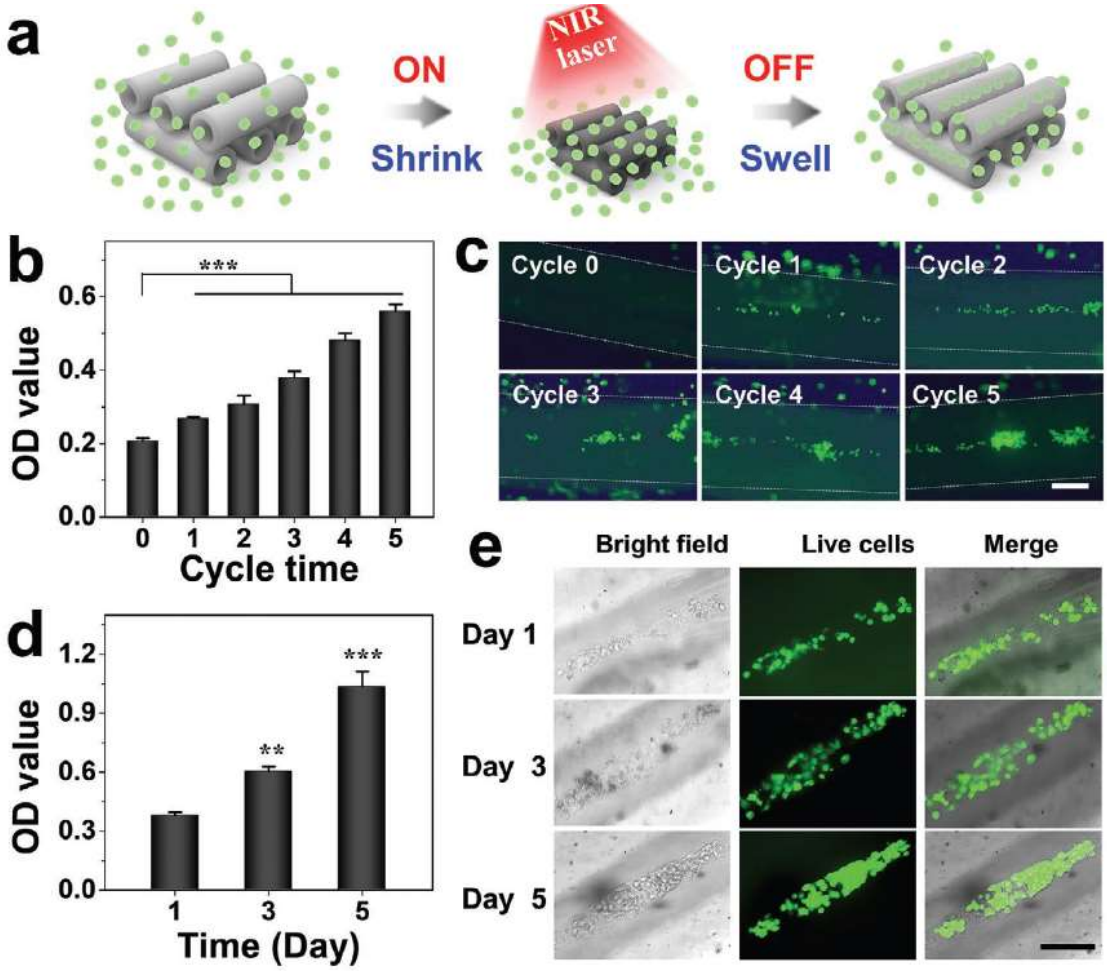

Fig. 3.8. a) Controlling of the channels size with NIR laser irradiation, b) quantitative diagram of OD value to cycle time, c) fluorescent images of human umbilical vein endothelial cells (HUVECs) for 0-5 cycles in the scaffolds, d) Cell proliferation diagram, e) morphologies of HUVECs in the scaffolds. Scale bars are 300 μm.

In our effort to go beyond the state of the art, we decided to go with a hybrid system that combines the strengths of additive and subtractive manufacturing, with the use of a commercial 3d printer and a laser source, as it will be discussed in the next chapter. This system allows for the creation of high-resolution (down to 50 microns) hierarchical structures, without altering the biocompatibility of the material. The creation of various sizing channels that will improve the delivery of oxygen and nutrients is possible with this technique and is being investigated as our next future step.

CHAPTER IV

Materials And Methods

4.1 Introduction

Commencing this chapter, the study that was done for the implementation of the system will be presented. First, the system architecture is described and it is divided into individual subsystems, then the system applications and the auxiliary software are described. Schematically, the device is summarized in Figure 4.1.

This section presents the analysis of the system and its division into subsystems in terms of architecture. The setup used includes a laser source, a commercial 3d printer, a computer, a galvo mirror and several mirrors to guide the laser beam.

The conditions of the laboratory were: steady temperature with climate control at 20-22 degrees Celsius and relative humidity 50%.

Three-dimensional scaffolds were created from the polymeric materials (e.g. PLA) in which, with the help of the laser, various designs were made, in order to study a variety of factors and how they affect the biological and physicochemical properties of the scaffolds. The samples' storing process was common, sealing them in airtight plastic containers to prevent dust accumulation or accidental damage. The parameters initially studied were the scanning speed of the sample as a function of the laser radiation power and the role they play in the morphology of the structures. An optimization of the printing process with respect to the printing speed, infill, nozzle and bed temperatures.

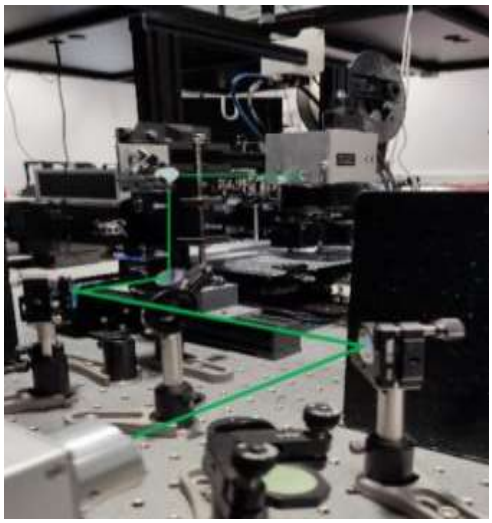

The parameters that remained constant after the optimization, throughout the research were:

- Experiment environment: Atmospheric, normal conditions.
- Pulse duration: τ_p = 5ns
- Pulse repetition rate: F = 1kHz.
- Laser wavelength: λ = 1060nm.
- Layer height H = 0.15 mm
- Print speed v = 10.5 mm/s
- Nozzle diameter d_n = 0.4 mm

Fig. 4.1. Laser beam pathing. Beam starts from the laser and is guided to the galvo through multiple flat mirrors. The galvo finally guides the beam to the platform where the sample lies.

4.2 Experimental Setup

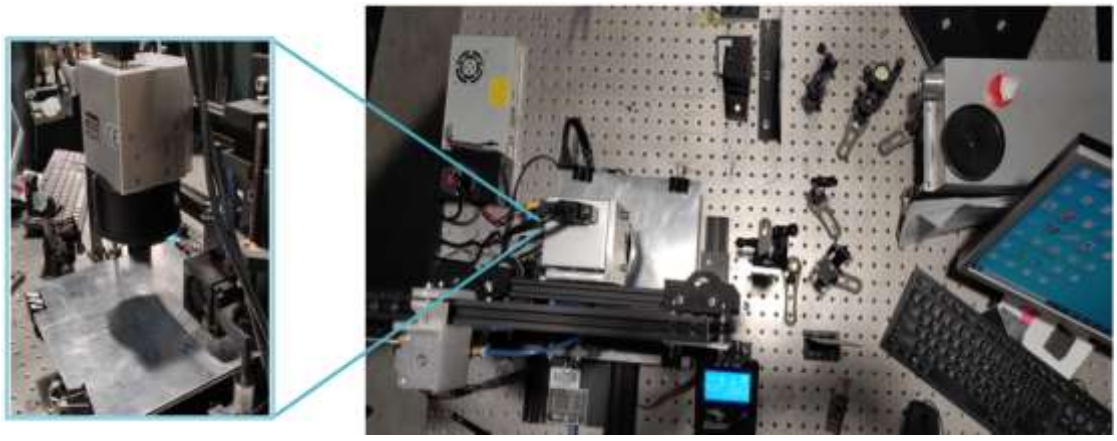

Fig. 4.2. Experimental setup consisting of our laser system, mirrors, galvo, 3d printer and computer.

The exact setup seen in fig. 4.2 is an IPG fiber Ytterbium picosecond laser with a galvo mirror and a commercial ender-3 3d printer. The whole system is controlled through a custom software and the advantages of this system are numerous. This system offers high resolution at relatively high speed and low cost. Also, a simple setup like this, with just a few mechanical parts, has very low vibrations so the procedure has no random errors due to the system, while we could also consider it portable. Galvo laser machines use high-speed, motor-driven mirrors to steer the laser beam through a lens. Depending on the position

within the laser marking field, the beam impacts onto the material at a greater or lesser angle of inclination. The marking field size is defined by the deflection angle and the focal length of the optics. Since there are no movable parts (with the exception of the mirrors) the laser beam can be guided over the workpiece at extremely high speeds with high precision and repeatability, making them ideal when short cycle times and high-quality markings are required.

4.2.1 Laser's software

LabVIEW is the IPG software used to control the laser. The software allows tweaking several different parameters and allows external control of the laser. It has 4 different APD modes for pulse duration 150ps, 1ns, 2ns, 5ns. The other parameters that can be controlled are a) the repetition rate (kHz), b) laser beam's power %, and c) prepump, as seen in fig. 4.3. A mode of LabVIEW allows one to externally control the laser. This way we linked our python custom software with LabVIEW, so laser is controlled from our gcode.

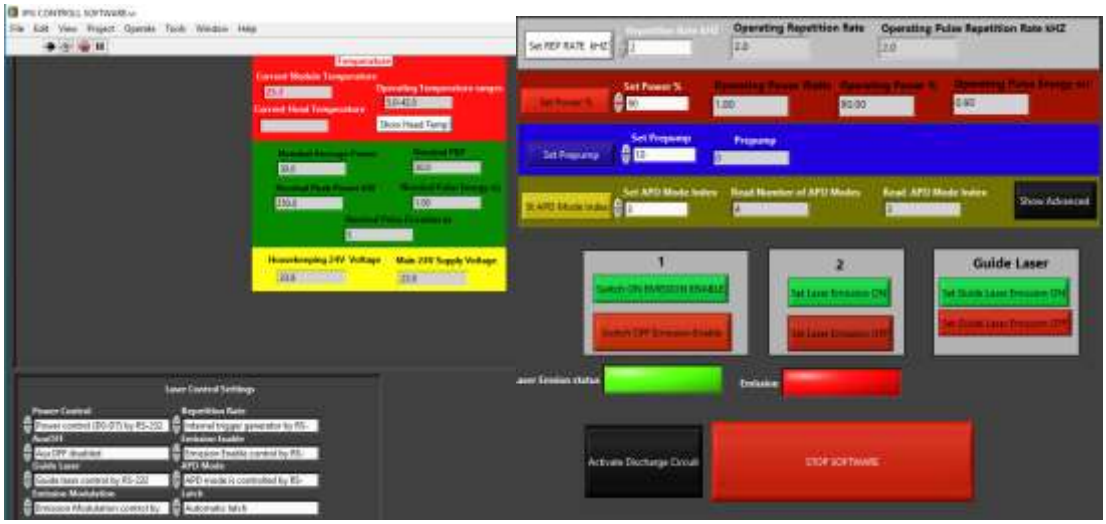

Fig. 4.3. Laser control software. This software allows for the manipulation of the laser's parameters.

4.2.2 Galvo-printer software

A custom software allows the cooperation of galvo and printer, resulting in a series of joint movements. This software allows us to move the printer's bed and the galvo mirror, while offering both manual and automatic operations, to create complex structures. The functions can be summarized as follows:

1. Manual operation

• Opening / closing the laser's shutter

• Number of total pulses

• Movement in 3 dimensions. Movements: Left, right, front, back, up, down

• Adjust step distance

• Speed adjustment in 3 dimensions X, Y, Z

• Setting a reference point

• Transport to the reference point

2. Automatic functions

• Lines: Adjust the overall length, width and height of the structure, pitch and axis rotation. Ideal function for creating lines, grids and generally structures without curves.

• Circle spots: This function is used to draw circular structures and has the ability to adjust the distance both between each pulse (spot) for each cycle and between the concentric circles of a structure.

• Gcode: In this function we enter a ready-made design that we have prepared in gcode. In this case, a combination of Fusion360 and Ultimaker Cura was used to design and customize the structure.

In the "3D Laser Printer" main window (fig.4.4), all the possible functions of the software exist. From the menu tab, one can load the 3d print and laser designs and spatially manipulate them. The selection of the mode and functions is also possible through this window, whilst several parameters of the laser are also adjusted from here.

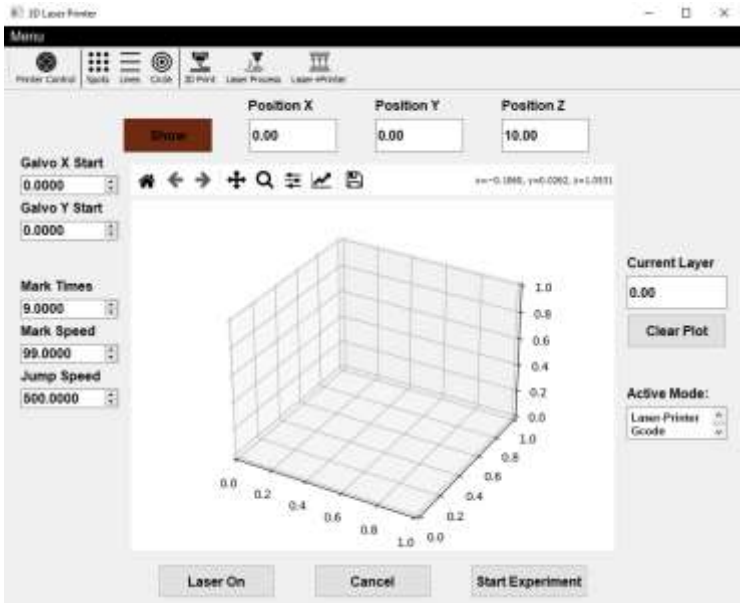

Fig. 4.4. Python custom software to simultaneously control the printer and laser.

The window of fig.4.5 allows the load of the 3d print design and the laser design, from the menu tab. The designs of the laser are assigned as plots, as seen at the left part of fig.4.5, and the manipulation of these plots is possible from this software. The active operations of the editor are a) duplication of the laser design, b) downscale of the laser design at the XY axes, and c) selection of the part of the 3d printed design that will be ablated, by customizing the initial and final ablation layer.

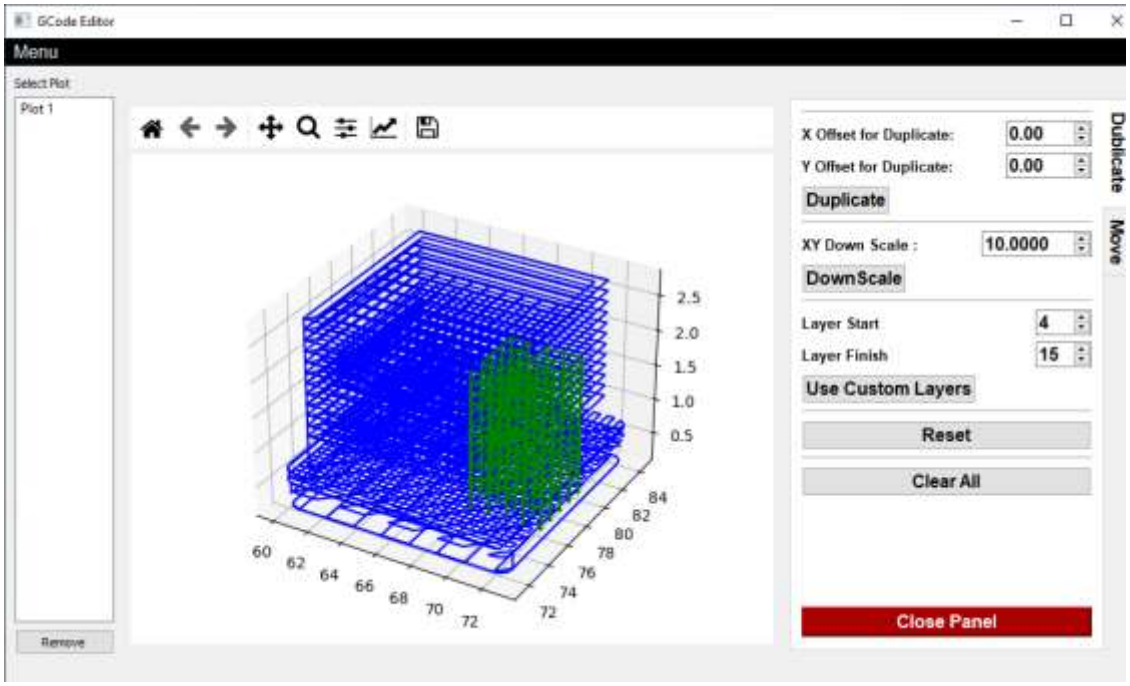

Fig. 4.5. Gcode editor window.

In fig.4.6 are seen the operations of the 3d printer one can do. These include the move of the hot end and of the bed, the move speed of these parts and their temperatures.

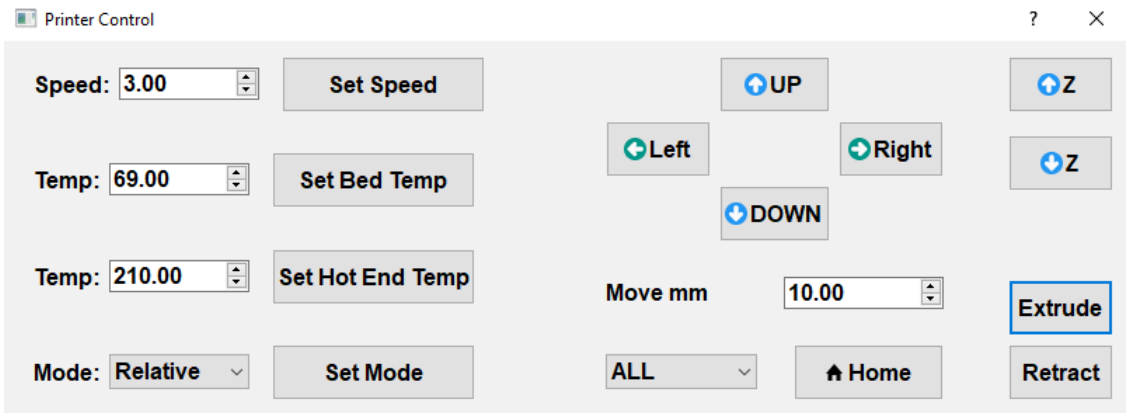

Fig. 4.6. Printer control window.

4.2.3 Fusion 360

Fusion 360 is a CAD software that allows the creation of very complex designs, as seen in fig4.5. The designs include but are not limited to grids, honeycomb or solid designs. Actually, the only limitation is our imagination. The complex design is translated to an STL format in order to be passed on the slicer software to make it gcode, providing the printer with the exact movements it must make.

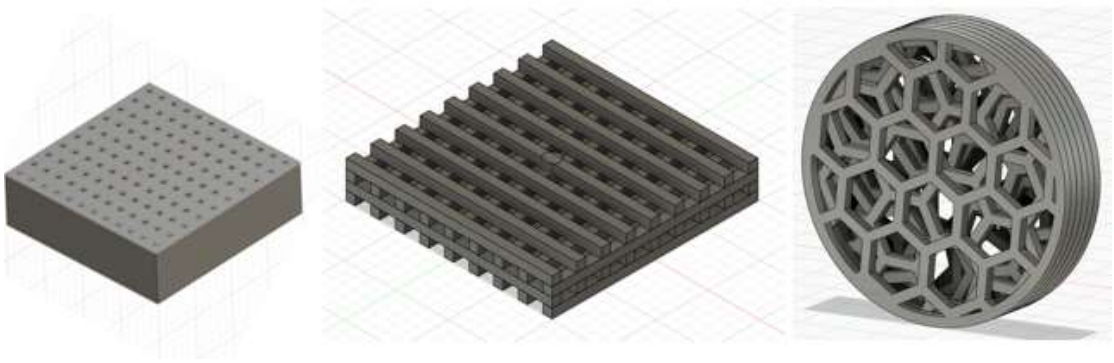

Fig. 4.5. A variety of complex designs using Fusion360. The same software is used to create the laser designs that is later translated through the python custom software.

4.2.4 Cura

Cura (fig4.6) is a software that slices our design in multiple 2D designs and translates it in gcode so that the printer gets the exact directions it must follow in order to create the final design as it was visualized at the CAD program.

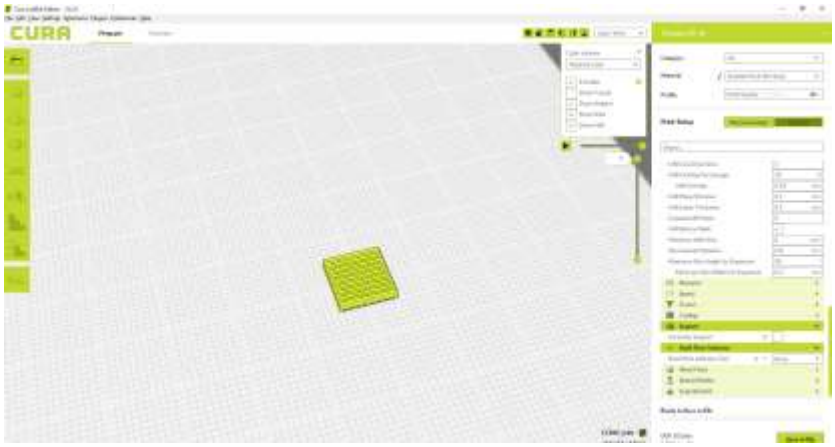

Fig. 4.6. The Cura Lulzbot user interface. Every possible parameter the printer follows is set here.

From Cura we can control parameters such as velocity, temperature, infill, fan, supporting structures and even enlargement or shrinking can be made. The exact parameters of the printing system are needed in order to ensure the correct guidance of the printing head and avoid bugs.

4.2.5 Pulse energy density

The pulse energy is not enough to characterize the experiment, as the focus of the beam and the surface covered by each pulse also play a role. As mentioned in Chapter 2, non-linear absorption mechanisms in transparent materials take place only at the focus point and not far from it. We first calculate the energy of a pulse E p by dividing the mean intensity of the P-beam, as measured by a power meter before the final concentrator, by the repetition rate of the pulses (f).

$$E_p = P / f \qquad (4.1)$$

The pulse radius can be calculated using the Gaussian distribution and by measuring the diameter of the structure created by a single pulse, with an optical microscope image or the device camera. From these two quantities we can calculate the energy density of the pulse.

4.2.6 Laser beam alignment

Before irradiating the material, it is essential that the beam is precisely aligned and focuses on the sample to be studied. The alignment of the beam was done in the first stage with the use of a special color card. Using an iris, we observed the shape of the beam, which should ideally be circular. If the shape deviates, the mirrors must be rotated properly, until the desired shape is achieved. Finally, using an aperture, the beam passes through the center of the lens. This procedure is necessary to achieve the maximum accuracy and homogeneity of the final beam that will hit the sample.

4.2.7 Focus of the laser beam

In order to find the best focus, the sample was irradiated with one pulse at a time, for different heights. The diameter of the spots was then measured under an optical microscope and the smallest position was selected. The procedure was repeated for verification.

4.2.8 Laser ablation process

The method we used to process the samples utilizes a simple principle in order to have enhanced results. The procedure involves printing one layer of material and then irradiating the sample with the laser, over and over again. By setting several parameters we can achieve very complex designs. Since the ablation takes places after every layer, we can make holes or engraving inside the materials structure. By utilizing this principle, we use the laser as a fourth dimension, thus making our scaffolds 4D.

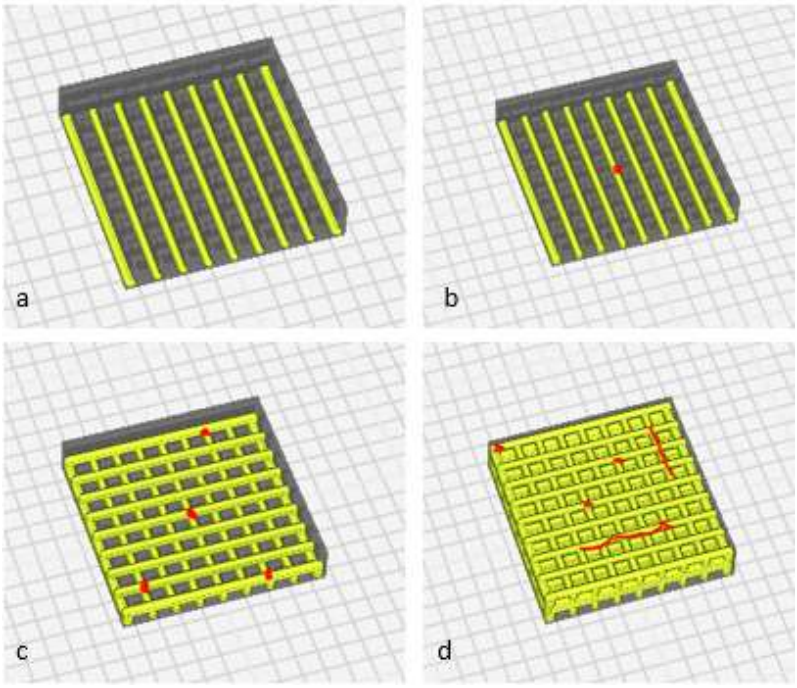

Fig. 4.7. a) first layer of the polymeric scaffold, b) second layer with a laser ablated hole, c) third layer with multiple laser ablated holes, d) fourth layer with laser ablated holes and lines.

4.2.9 Centering

In order to achieve best results, centering of the printed scaffold with the galvo mirror that is responsible for the targeting of the material with the laser beam (fig 4.8).

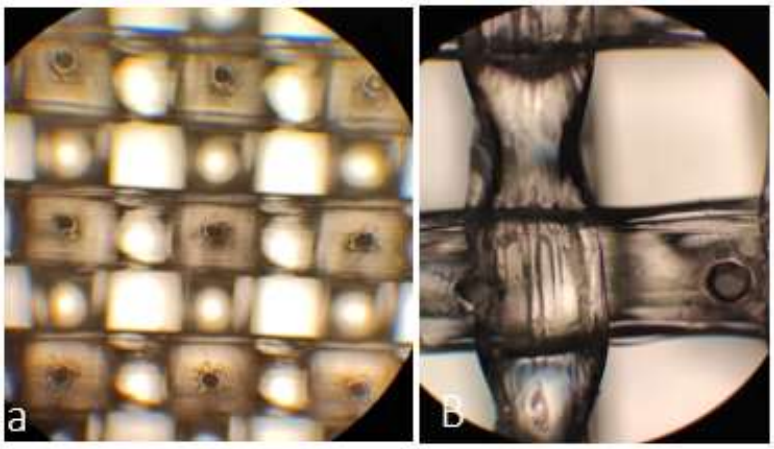

Fig. 4.8. a) well centered and b) bad centered printer – laser beam system.

4.3 Materials

4.3.1 Polylactic acid (PLA)

The material used was a commercial natural PLA filament of 1.75 mm thickness from PrimaCreator. The filament used as is, without special preparation, treatment or storing. Natural PLA is transparent and its advantage to colored PLA filaments is that the former is biocompatible and non-toxic.

4.3.2 Polycaprolactone (PCL)

The PCL material obtained in pellet form (~3mm) from Sigma-Aldrich. The number average molecular weight of the polymer is M_m = 80.000. The PCL's filament was created from the pellets using a heat extruder. The temperature at which optimal extrusion was observed was T_e = 100 °C.

4.3.3 Cellulose Acetate (CA)

The CA was used only as a composite with PCL in 10% (wt%) concentration. CA was obtained from sigma Aldrich in powder form and the number average molecular weight of the polymer is M_m = 30.000. PCL pellets were mixed with CA powder in the same extruder, but the optimal extrusion temperature was T_e = 140-160 °C.

4.3.4 Heat extrusion

To create the custom filament, the heat extruder of fig 4.9 was used. It is a process that involves the insertion of the material in a mixing chamber.

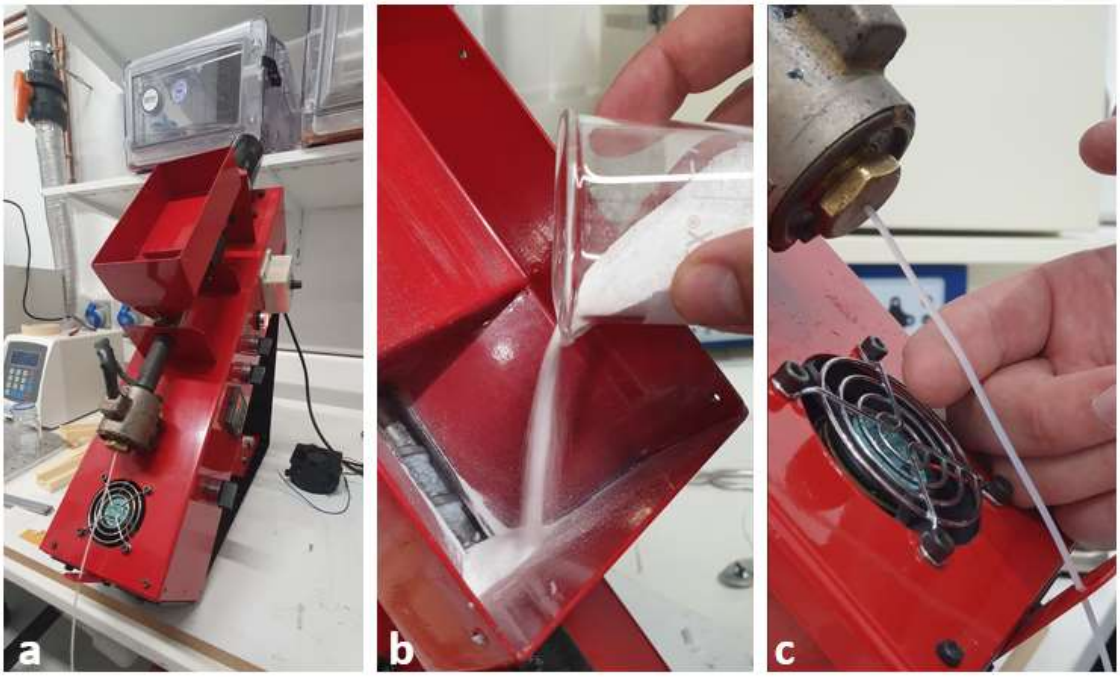

Fig 4.9. a) Heat extruder, b) material insertion chamber, c) close-up view of the resulting filament

The material is then transferred through a mill at the heater, where the material is melted and is then pushed out of the machine, through a narrow hole. The material in its thread form is then cooled down in room temperature and rolled.

The heat extruder was provided by dr. Kenakakis George (PPM group LAB). The procedure was conducted under the supervision of dr. Viskadourakis Zacharias, together with Ntoulias Christos and Daskalakis Panagiotis.

4.4 Characterization of the samples

4.4.1 Structural and Morphological characterization via Scanning Electron Microscopy (SEM)

The collection of images was taken at FESEM of the University of Crete (JEOL, JSM-7000F), where we selected the appropriate magnification and focus of the images with the help of the scientific staff. An important part of the process is to have a sample without residues and impurities, which would prevent a sufficient vacuum for collection. Equally important is the sputter coating of the samples. Sputtering took place at the premises of the University of Crete, on the instrument Sputter-coater scd 050 (Fig. 4.4), in order to coat gold on their surface. The thickness of the coating follows the values of the diagram in the figure, while the parameters that can be adjusted are the electrical intensity of the device and the time that the sputtering lasts. All of our samples were sputter coated with gold (Au) for 39 sec and 40 mA, to create a conductive10nm thick layer (as shown in Fig. 4.4).

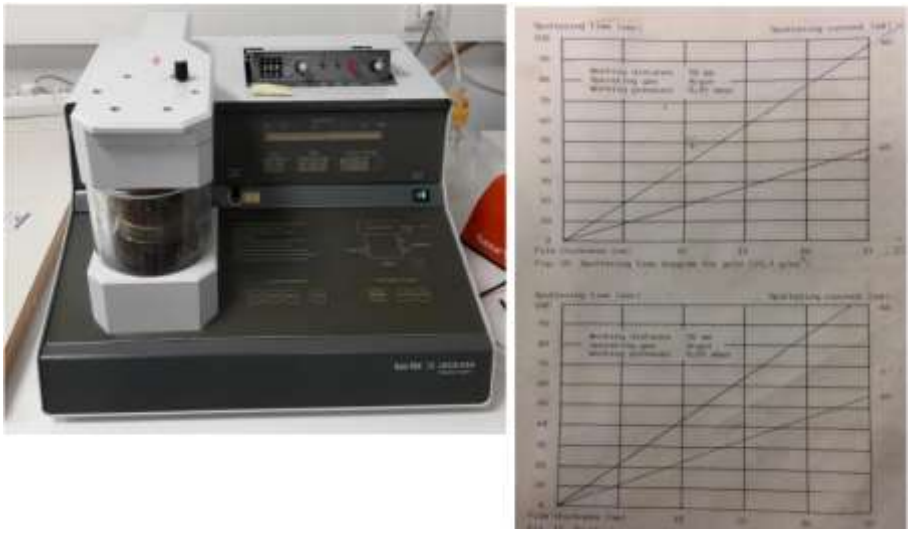

Fig. 4.9. Left: Coating instrument Sputter-coater scd 050. Right: Coating time - thickness diagrams regarding current intensity, for gold and gold/palladium coatings

4.4.2 Preliminary Cell Study on 3D and 4D printed scaffolds

For all cell cultures at this preliminary study, mouse NIH 3T3 fibroblasts, SW10 and Mesenchymal Stem Cells were used. The main objective was to investigate the effect of these scaffolds on cell adhesion and proliferation and at the same time to observe the cell morphology affected by the scaffolds. The ability of cells to sense their neighboring environment and the 3D/4D scaffolds (mechanotransduction) was also assessed.

Murine cell line - NIH 3T3

The murine cell line NIH 3T3 has been used as a cytotoxicity/cytocompatibility model system in biomaterials' studies. It was established in 1963 from Mus musculus f. domenstica ("Swiss mouse") embryo fibroblasts. The cells, which immortalized spontaneously, were designated "3T3" according to "3-day transfer, inoculum 3 × 105 cells" [71]. "NIH" for "National Institutes of Health" was added later.

Schwann mouse cell line - SW10

The Schwann (SW10) mouse cell line, is an established adherent neuronal Schwann cell line; immortalized with SV40 large T antigen. SW10 cells were obtained from ATCC® (CRL-2766).

Mesenchymal Stem Cells -MSCs

Mesenchymal stem cells (MSCs) are adult cells that differentiate into various tissues including, but not limited to, bone, cartilage and adipose cells. Great anti-inflammatory and generally therapeutic effects are linked with this type of cells.

General Culturing Conditions: The cells were grown in cell culture flasks using Dulbecco's modified Eagle's medium (DMEM) – High glucose (4500mgr/L glucose) supplemented with 10% fetal bovine serum (FBS) and 1% penicillin/streptomycin solution (PS) at 37°C in a 5% CO2 incubator, with medium renewal every 3 days. All cells used for the experiments were in a passage, ranging from 7-10. All scaffolds were UV sterilized and transferred into sterile wells of 24-well plates. 50000-100000 cells/ml in culture medium were seeded on the samples and were cultured for 1 and 3 days (for the fibroblasts and Schwann cells), and 2 and 4 days (for the MSCs). Tissue culture plastic (TCP) coverslips were the control samples (reference material) in all the experiments.

A cell study on 3D and 4D PLA, PCL and PCL/CA scaffolds seeded with MSCs (passage 10) was conducted for 2 and 4 days at two different experiments, and on two samples per sample group to ensure reproducibility of results. The 3D and 4D PLA scaffolds were of 10.45x10.45x1.8 mm (LxWxH) total dimensions and every 3d printed line was spaced 0.55 mm from its next. The 4D design (holes of 0.07 mm diameter) was made through laser ablation at 5 ns pulse

duration, 2 kHz pulse repetition rate and 1.98 W power. Characterization was conducted through SEM (UoC – Biology Department) and confocal imaging. The sample preparation for SEM and Confocal Imaging are described below.

Scanning electron microscopy: preparation of the biological samples -dehydration procedure

The cells growing on the scaffolds and TCP samples were analyzed by the SEM microscope (JEOL). After each time point, the cells were fixed following a specific fixation protocol. The medium was removed from samples and they were washed twice with 0,1M Sodium Cacodylate Buffer (SCB) (pH = 7,4) for 5 min in 4oC. Then they were fixed with 2,5% glutaraldehyde (GDA) / 2,5% paraformaldehyde (PFA) in SCB fixative buffer for 30 min at 4oC. The samples were then washed twice (for 5 min each time) with 0,1M SCB at 4oC. The samples at dehydration phase were washed in graded series of 30%, 50%, 70%, 90%, and 100% EtOH for 10 min each at 4oC. Then, the samples were transferred into a chemical hood and immersed in hexamethyldisilazane (HDMS)/ EtOH (50:50) solution for 30 min and 20 min, then, in 100% HDMS for 20 min twice at 4oC. As a final step, HDMS was removed, and samples left to dry completely overnight at the chemical hood. Prior to electron microscopy examination, the samples were sputter-coated with a 15nm film of Au (BAL-TEC SCD 050).

Confocal microscopy: Immunostaining protocol for preparation of the biological samples

For this assay, the medium was removed from samples and they were washed twice with Phosphate Buffered Saline (PBS) 1x (pH = 7.4) for 5 min and then fixed with 4% paraformaldehyde (PFA) for 15 min at RT. After removal of PFA solution, the samples were washed again twice with PBS 1x and treated with Triton-X100 0,1% solution in PBS for 5 min in order to permeabilize cell membranes. Then, the samples were washed twice with PBS 1x for 5 min and blocked using 2% Bovine Serum Albumin (BSA) in PBS solution for 30 min. Subsequently, the cells incubated with the first antibody overnight at 4oC. Next day, the cultured cells washed twice with PBS 1x and incubated with the secondary antibody and actin phalloidin 568 or 680 (1:500) for 2 h and then nuclear staining carried out by 4,6-diamidino- 2-phenylindole (DAPI 1:10.000 in PBS) at RT. The first and second antibodies used in the present study were vinculin (1:500, 1st and 2nd antibody_488nm) and TAZ (1:500, 1st and 2nd antibody_488nm or 647nm). Both 1st and 2nd antibodies were diluted in 1% BSA in PBS 1x solution, at the respective concentrations. The samples were transferred on microscope slides for observation using a 'Leica SP8' laser scanning confocal microscope.

Cell study on proliferation, morphology and mechanotransduction of the 3D and 4D PLA Scaffolds	**Cell study on adhesion, proliferation and of the 3D and 4D PCL Scaffolds**	**Cell study on adhesion, proliferation, morphology and mechanotransduction of the 4D PCL and PCL/10% CA Scaffolds**
NIH 3T3 fibroblasts / SW10 cells / MSCs (50.000 cells/ml or per sample) **Time point:** 1 and 3 days; and 2 days (for MSCs) **Samples:** TCP Control, PLA flat (3D), 4D PLA scaffolds with holes, 3D PLA (bulk) with rectangular ablated areas of different depth **Main objective:** To investigate the effect of these scaffolds on cell adhesion and proliferation	MSCs, Passage 13 (100.000 cells/ml or per sample) **Time point:** 2 and 4 days **Samples:** TCP Control, PCL (3D), 4D PCL scaffolds with holes **Main objective:** To investigate the effect of these scaffolds on cell adhesion and proliferation	MSCs, Passage 10 (80.000-100.000 cells/ml or per sample) **Time point:** 2 and 4 days **Samples:** TCP Control, 3D scaffolds, 4D scaffolds with holes **Main objective:** To investigate the effect of these scaffolds on cell adhesion and proliferation
SEM imaging	**SEM imaging** **ImmunoStaining procedure** for observation under Confocal Microscope: DAPI for cell nucleus (cell proliferation), Actin Phalloidin @TRITC 532nm for cytoskeleton (cell morphology and orientation) & & Vinculin antibody @ 488nm represents the focal adhesion points on the cytoskeleton	**ImmunoStaining procedure** for observation under Confocal Microscope: DAPI for cell nucleus (cell proliferation), Actin Phalloidin @568 and 680nm for cytoskeleton (cell morphology and orientation) & TAZ antibody @ 488 and 647nm for assessment of mechanotransductive role and it can be localized in nucleus, or cytoplasm, or both & Vinculin antibody @ 488nm represents the focal adhesion points on the cytoskeleton

Table 4.1. All the specific experimental conditions per cell study are listed (these studies were performed by Ms E. Kanakousaki, MSc student and Ms P. Kavatzikidou, Postdoctoral researcher).

CHAPTER V

Results and Discussion

5.1 PLA scaffolds 4D printing

Natural PLA filament is transparent, thus high photon energy is needed to degrade the material, since our beam's wavelength corresponds to lower energy that that of the material's energy gap.

For very low energy power, no degradation of the material was observed, while for very high the laser beam penetrated the material. The scope of this study concerns the intermediate power, which was able to decompose material from each layer of the sample without corrupting the other layers. For the laser's parameters, multiple scan times were used, depending on the designs, velocity and energy power in the range 2-3 W. All of the parameters are concentrated on table 5.1. All the following SEM images were taken and edited from ms. Aleka Manousaki.

The experiments were done with constant pulse duration τ_p = 5 ns, repetition rate f = 3 kHz, power P = 2,4 W, mark ablation repetition N = 2 and mark speed v_m = 50 mm/s. The layer height of the design is H=150μm and width W=450μm.

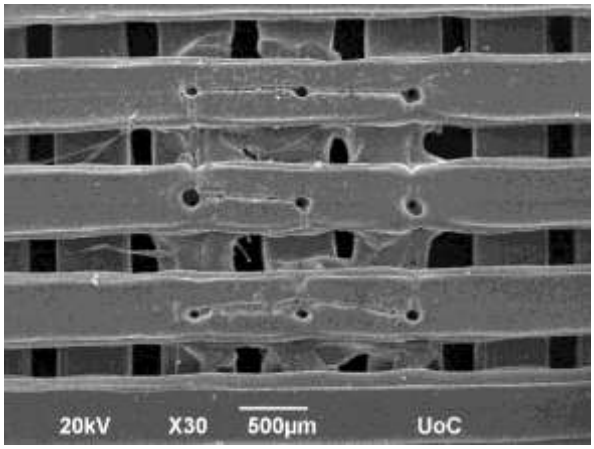

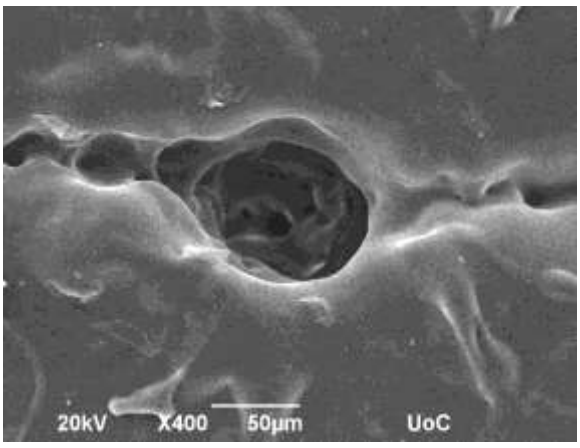

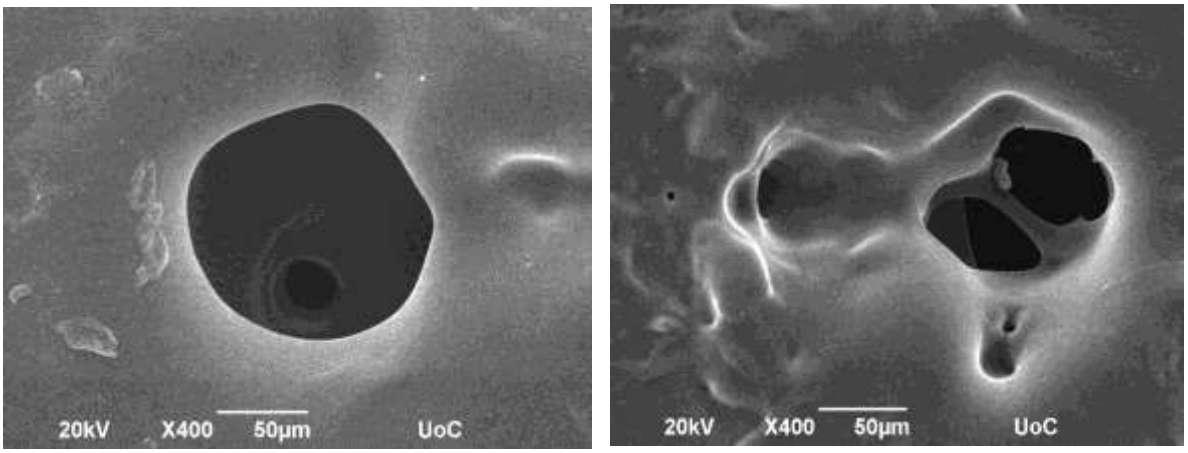

Fig. 5.1. SEM images for holes design with cura's ready gcode. Parameters used were τ_p= 5ns, f = 3khz, P = 2,4 W, 2 marks, mark speed = 50 mm/s, jump speed = 500 mm/s.

The first sample's (fig. 5.1) dimensions are 10x10x1.8 mm. The strands width and height are both 450 μm and the strand spacing used is about 250 μm, varying by 10% due to thermal effects on the polymer used. The holes diameters varied from 70 to 100 microns, with the higher end probably being due to "laser's pathing". "Laser's pathing" is a phenomenon appearing due to the gcode movements extracted from Cura, in which the laser does not stop irradiating when moving from one hole to the other. This phenomenon is fixed by using our own custom gcode instead the "readymade" of Cura. We observe that for power P = 2,4 W and repetition N = 2 the holes weren't completely hollow. This leads to the conclusion that we need higher ablation rates in order to make see-through holes. To achieve this, we increased the repetitions, as this is the way to better results, although slower than just increasing the laser's power.

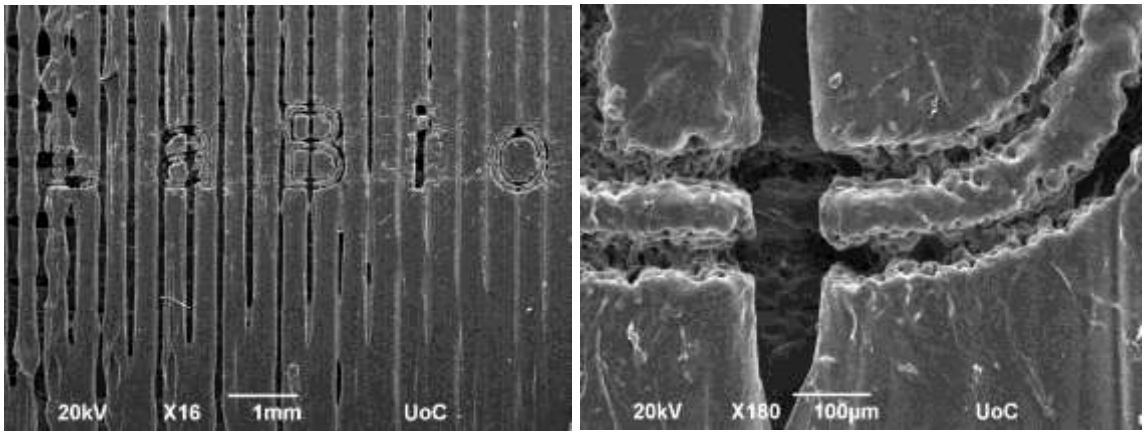

Fig. 5.2. SEM images for "LaBio" design. Parameters used were τ_p= 5ns, f = 3khz, P = 2,4 W, 2 marks, mark speed = 50 mm/s, jump speed = 500 mm/s, thin extrude width = 30 μm.

Another 3D design tested is “LaBio” (fig. 5.2) and is a complex design created in fusion360 using the text function and thin extrusion with width W=0.3 mm. As seen in the SEM images the design is precise and microstructures are made inside the ablated channels, but more adjustments need to be made, as due to thermal effects, cracks were inflicted to the scaffold’s surface. More complex designs will uncover the limits of our system.

As seen in fig. 5.3, the final results were much better than the first ones. In order to achieve this, we eliminated the laser’s pathing as it did lead to inconsistent results, lowered the power to P = 1.9 W and increased the ablation repetition to N = 10, as this was found to be the least number of repetitions needed to pierce the PLA at the parameters used. The sample’s dimensions are 10.45 x 10.45 x 1.8 mm. The strands width and height are 450 μm and the strand spacing used is about 550 μm. The holes of diameter 70 μm are made in the cross sections of the strands in order to create higher porosity. Calculations in respect to the parameters used show that every repetition ablated an area of A = 0,4 cm^2 and had depth D = 15 μm. The layer height of the design is H=150 μm and width W=450 μm, whilst the nozzle diameter was 0.4 mm.

The 4D PLA scaffolds discussed above are concentrated on the table 5.1, along with the processing parameters.

Sample	Pulse duration	Repetition rate	Power	Mark times	Speed
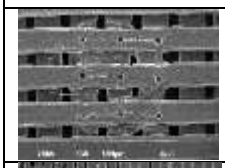	5 ns	3 kHz	2,4 W	2	50 mm/s
	5 ns	3 kHz	2,4 W	2	50 mm/s
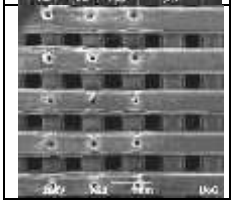	5 ns	2 kHz	1,98 W	10	100 mm/s

Table 5.1. Concentrated laser ablation parameters for the different PLA scaffolds.

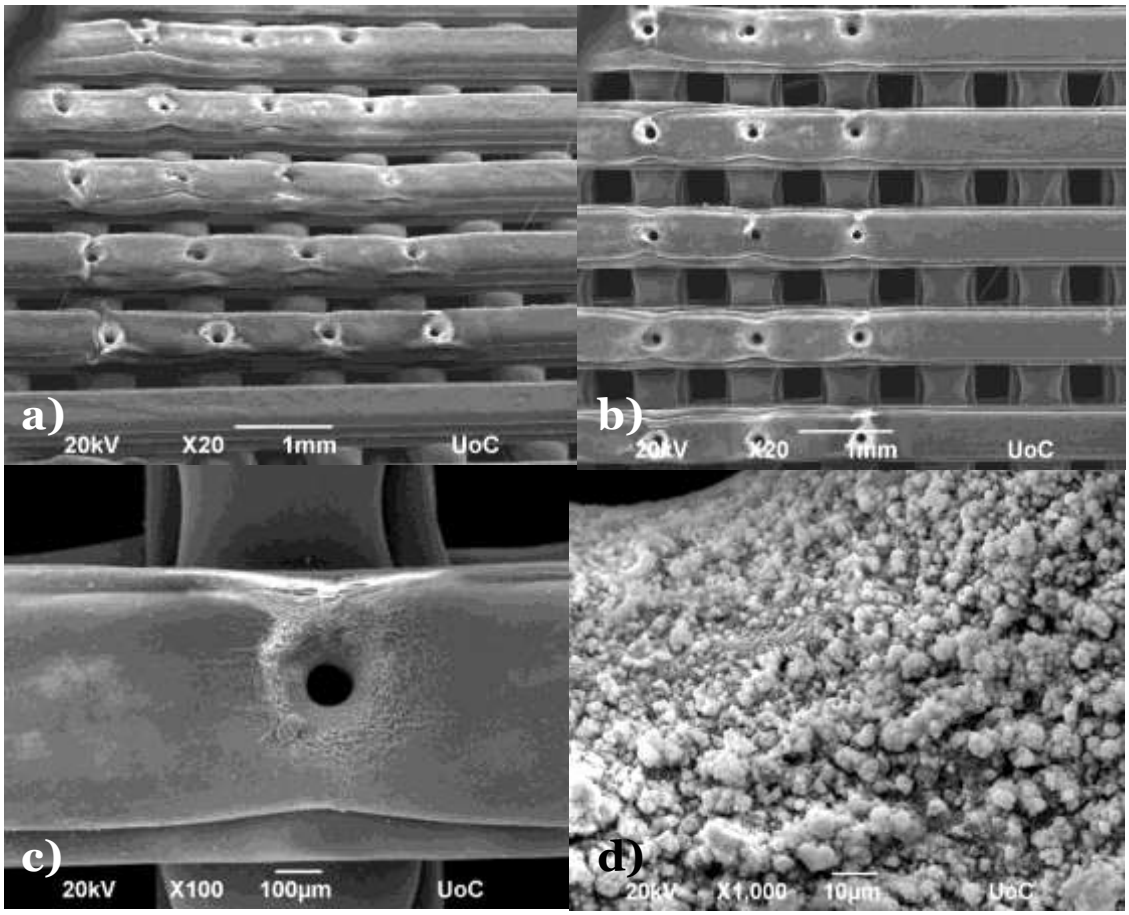

Fig. 5.3. Sem images for grid design with 20 holes made by laser ablation. a) 45° tilted view of the design, b) above view of the design and non-ablated material, c) laser ablated hole, d) microstructures around the ablated hole.

Although we present only selected samples in this thesis, several PLA scaffolds were made to ensure reproducibility. Some of them were taken to the SEM for characterization and the others were used for cell culturing.

Some of the 4D PLA scaffolds shared a decolorization, like the one we can observe at fig. 5.3a. This could be due to non-homogenous sputtering and the white color we observe actually means low gold particles concentration at this area. The non-conductive PLA acts as an electron trap, so at this area the so-called "charging" (accumulation of electrons on the surface) creates extra-white regions.

5.2 4D printed PCL scaffolds

For very low energy power, no degradation of the material was observed, while for very high the laser beam penetrated the whole material. The scope of this study concerns the low - medium power, just like in the case of PLA, which was

able to decompose material from each layer of the sample without corrupting the other layers. For the laser's parameters, multiple scan times were used, depending on the designs, velocity and energy power in the range 1-2 W.

The sample's dimensions are 10.45 x 10.45 x 0.9 mm. The strands width and height are 450 μm and the strand spacing used is about 380 μm. The holes of diameter 70 μm are made in the cross sections of the strands in order to create higher porosity. Calculations in respect to the parameters used show that every repetition ablated an area of A = 0,4 cm^2 and had depth D = 15 μm. The experiments were done with constant pulse duration τ_p = 5 ns, repetition rate f = 2 kHz, power P = 1.8 W, mark ablation repetition N = 15 and mark speed v_m = 50 mm/s. The layer height of the design is H=150 μm and width W=450 μm, whilst the nozzle diameter was 0.4 mm.

The 4D PLA scaffolds discussed above are concentrated on the table 5.1, along with the processing parameters.

5.3 Preliminary Cell Study on PLA scaffolds

5.3.1 Murine cell line - NIH 3T3

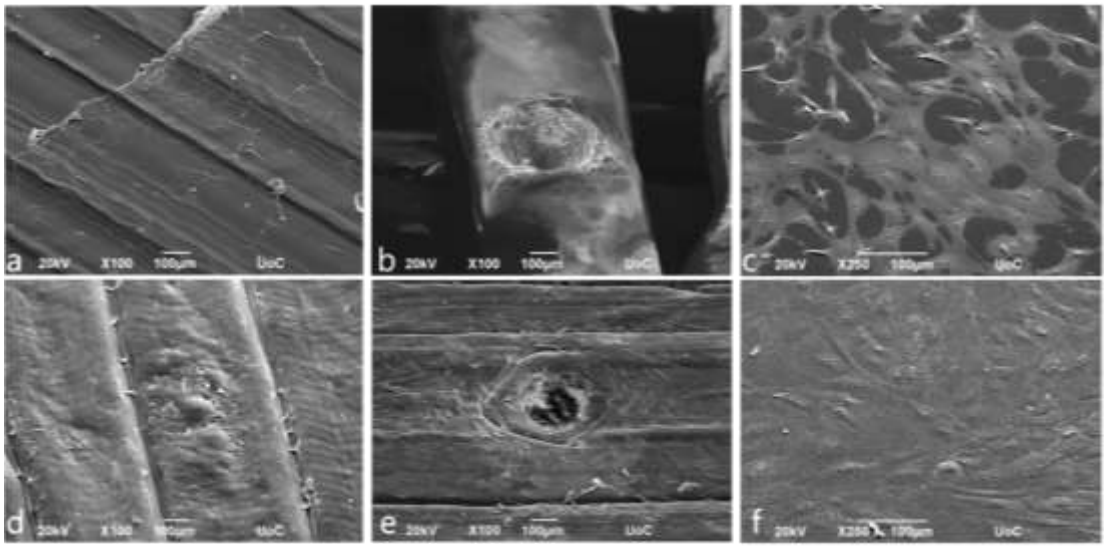

Fig. 5.4. Top and tilted view SEM images of PLA Scaffolds and TCP flat control surface (10.45x10.45mm with space distance 0.55mm with 20 laser ablated holes with 5ns, 2KHz, 98% and 1.98 Watts and hole diameter of 70 μm) with NIH 3T3 fibroblasts for 1- and 3-days culturing (cell concentration 50000 cells/ml or sample). a) 3D PLA scaffold after 1 day of cell culturing, b) 4D PLA scaffold after 1 day of cell culturing, c) TCP flat surface after 1 day of cell

culturing, d) 3D PLA scaffold after 3 days of cell culturing, e) 4D PLA scaffold after 3 days of cell culturing, f) TCP flat surface after 3 days of cell culturing.

The main observation from the SEM images of Fig. 5.4 is that the fibroblasts attached well and proliferated (for both time points) on the PLA scaffolds (flat surface of the 4D PLA scaffold) and around the hole, while there are some signs of fibroblasts entering the hole mainly at 3 days.

5.3.2 Schwann mouse cell line - SW10

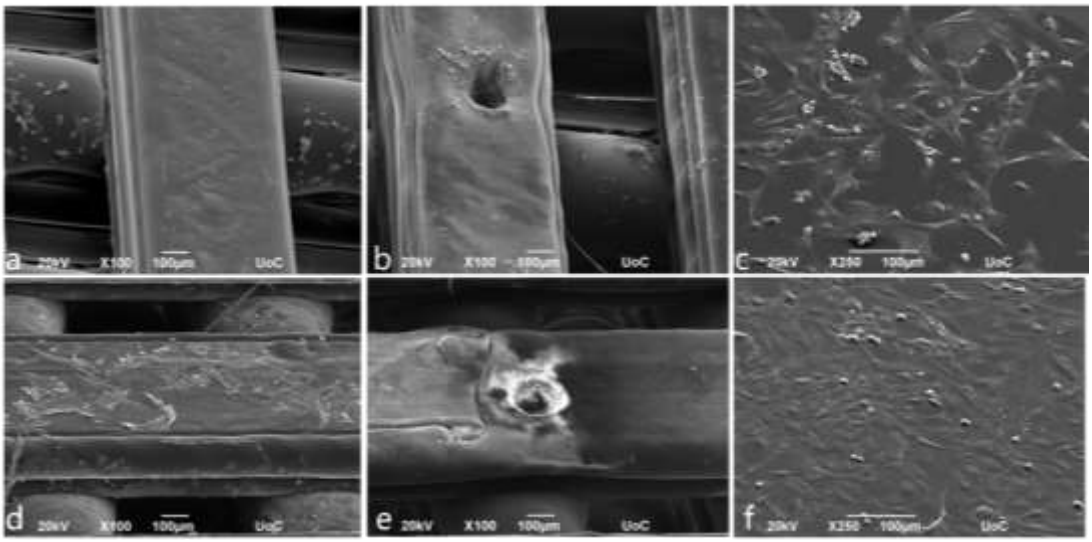

Fig. 5.5. Top and tilted view SEM images of PLA Scaffolds and TCP flat control surface (10.45x10.45mm with space distance 0.55mm with 20 laser ablated holes with 5ns, 2KHz, 98% and 1.98 Watts and hole diameter of 70 mm) with SW10 cells for 1- and 3-days culturing (cell concentration 50000 cells/ml or sample). a) 3D PLA scaffold after 1 day of cell culturing, b) 4D PLA scaffold after 1 day of cell culturing, c) TCP flat surface after 1 day of cell culturing, d) 3D PLA scaffold after 3 days of cell culturing, e) 4D PLA scaffold after 3 days of cell culturing, f) TCP flat surface after 3 days of cell culturing.

The SEM images of Fig. 5.5 demonstrated that the SW10 cells adhered and grew on the PLA scaffolds at 3 days and mainly on the flat surface. SW10 cells appeared not to adhere well to the holes of the 4D PLA scaffolds so a change in the laser ablation parameters is being investigated.

5.3.3 Mesenchymal Stem Cells

5.3.3.1 Culturing on PLA samples

The SEM images indicate that MSC cells have the ability to adhere and proliferate on the TCP flat, as well as on the 3D and 4D PLA surfaces. The proliferation of the cells is higher on the 3D printed surface than close and inside the 4D structure. Nevertheless, the cells are growing on the 4D surface in slower rates. Further investigation is needed on why and if the laser parameters affect these results.

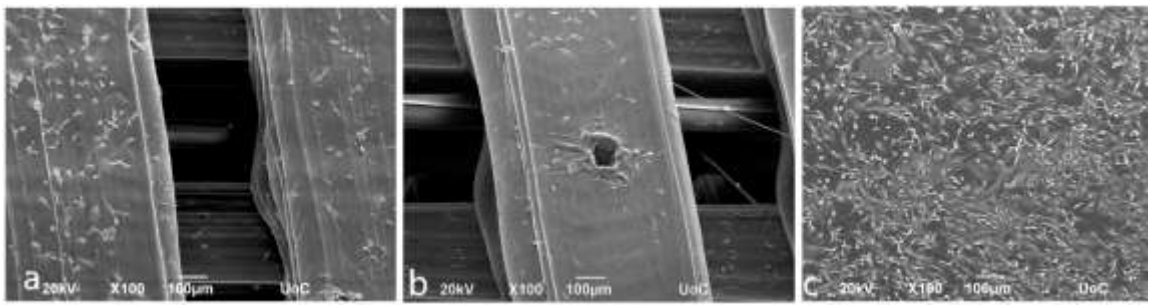

Fig. 5.6. Top and tilted view SEM images of PLA Scaffolds and TCP flat control surface (10.45x10.45mm with space distance 0.55mm with 20 laser ablated holes with 5ns, 2KHz and 1.98 Watts and hole diameter of 70 um) with MSC cells for 2 days culturing (cell concentration 50000 cells/ml or sample). a) 3D PLA scaffold after 2 days of cell culturing, b) 4D PLA scaffold after 2 days of cell culturing, c) TCP flat surface after 2 days of cell culturing.

5.3.3.2 Culturing on PCL samples

The SEM images indicate that MSC cells have the ability to adhere and proliferate on the TCPwhich can be characterized as a 2D substrate, as well as on the 3D and 4D PCL surfaces.

The proliferation of the cells is higher on the 3D printed surface than close and inside the 4D structure at 2 days. However, the cells at 4 days grown and covered the surface of the hole on the 4D scaffolds. A carpet-like cell layer covered the 3D and 4D PCL flat areas of the scaffolds at 4 days. The main MSC cell morphologies include cells that are flattened and enlarged and bipolar/tripolar-

shaped cells with not a specific orientation, appeared clearly at 2 days.

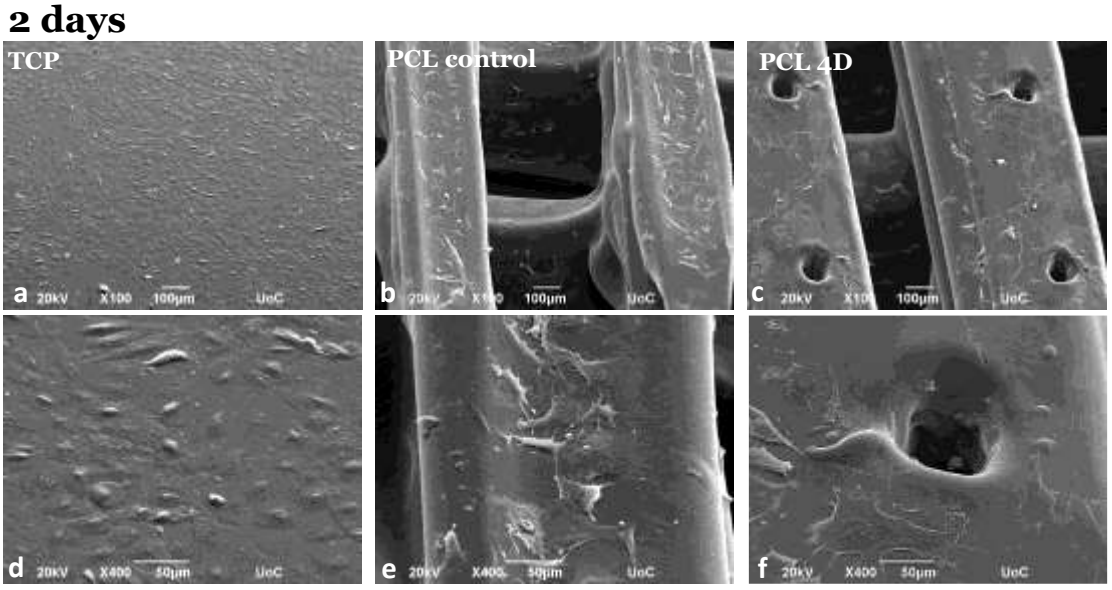

Fig. 5.7. Tilted view SEM images of PCL (3D and 4D) Scaffolds and TCP flat control surface (10.45x10.45mm with space distance 0.38 mm with 9 laser ablated holes at 5 ns, 2 kHz and 1.98 W and hole diameter of 70 um) with MSC cells for 2 days culturing (cell concentration 10^5 cells/ml or sample)at two different magnifications (x100 and x400) a) TCP flat surface after 2 days of cell culturing (x100), b) 3D PCL scaffold after 2 days of cell culturing (x100), c) 4D PCL scaffold after 2 days of cell culturing(x100), d) TCP flat surface after 2 days of cell culturing (x400), e) 3D PCL scaffold after 2 days of cell culturing (x400) and f) 4D PCL scaffold after 2 days of cell culturing (x400).

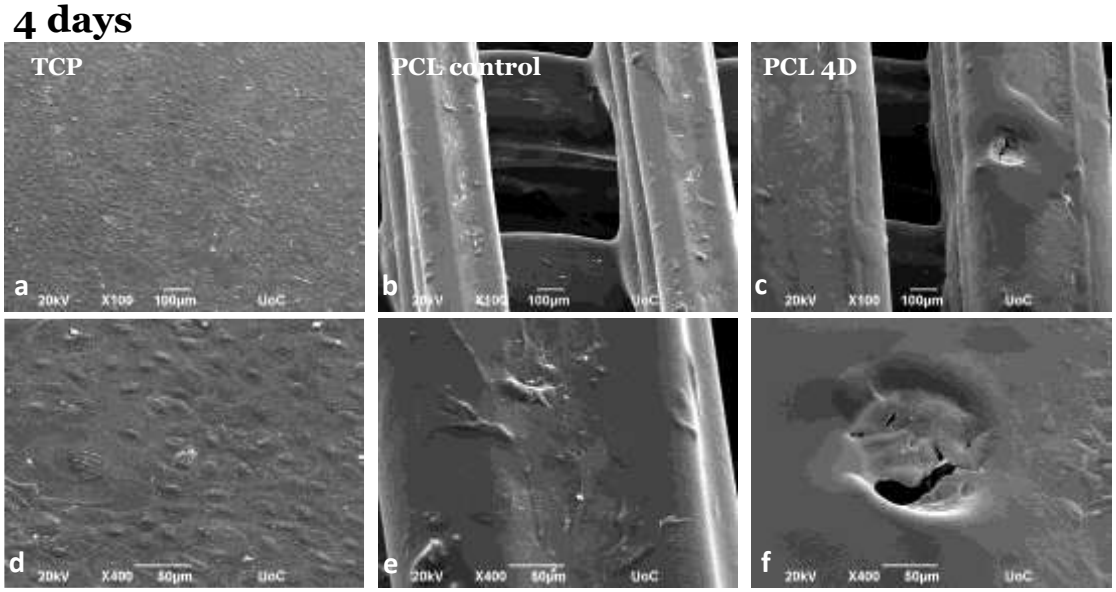

Fig. 5.8. Tilted view SEM images of PCL (3D and 4D) Scaffolds and TCP flat control surface (10.45x10.45mm with space distance 0.38 mm with 9 laser ablated holes at 5 ns, 2 kHz and 1.98 W and hole diameter of 70 um) with MSC cells for 4 days culturing (cell concentration 10^5 cells/ml or sample)at two different magnifications (x100 and x400) a) TCP flat surface after 4 days of cell

culturing (x100), b) 3D PCL scaffold after 4 days of cell culturing (x100), c) 4D PCL scaffold after 4 days of cell culturing(x100), d) TCP flat surface after 4 days of cell culturing (x400), e) 3D PCL scaffold after 4 days of cell culturing (x400) and f) 4D PCL scaffold after 4 days of cell culturing (x400).

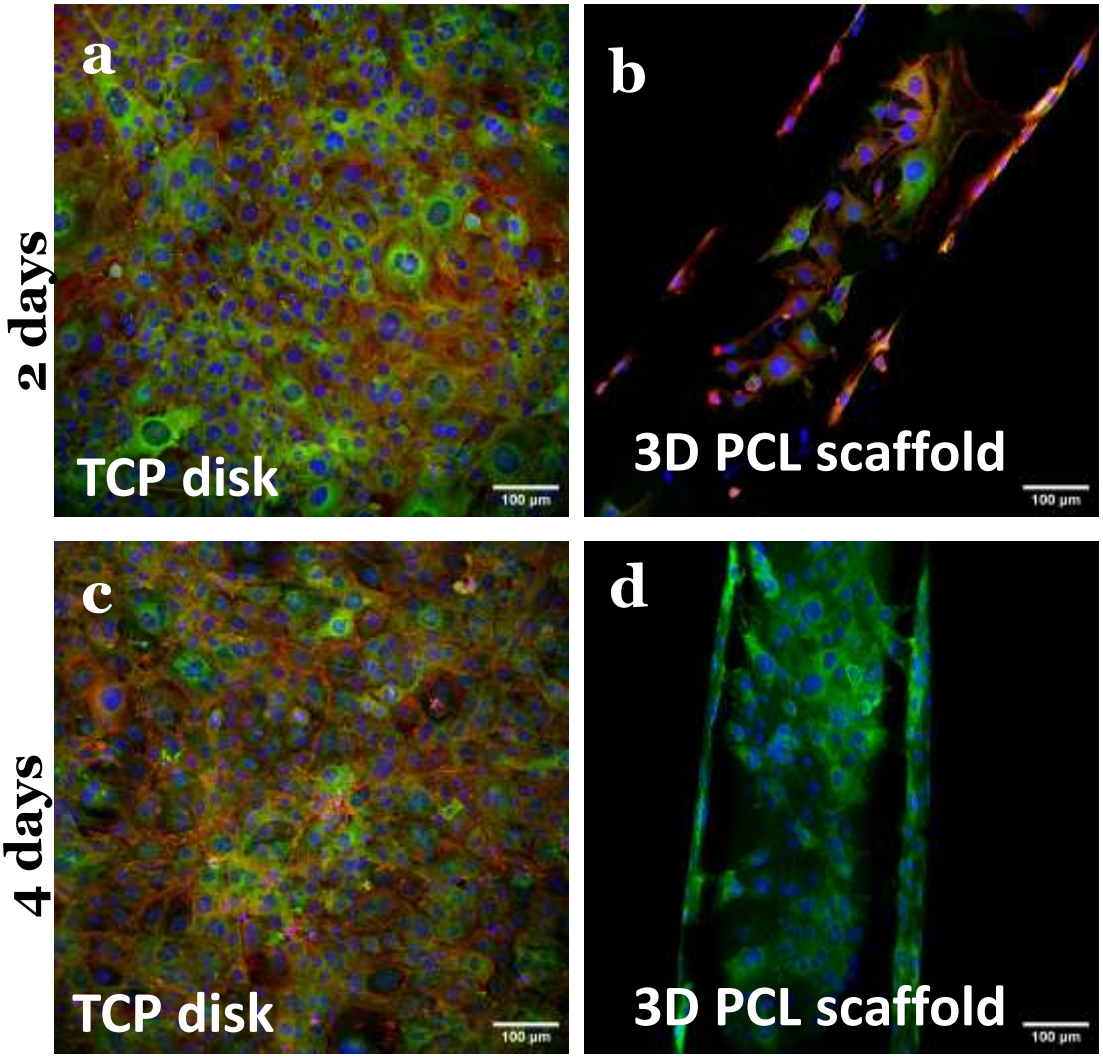

Figure 5.9A: Confocal images of Tissue Culture Plastic (TCP) disks (control) with MSCs cultured (a) for 2 days and (c) for 4 days, and 3D PCL scaffolds with MSCs cultured (b) for 2 days and (d) for 4 days. In blue colour is the DAPI, representing the MSCs nucleus, Vin 488 (1:500, 1st and 2nd antibody) (green colour) represents the focal adhesion points on the cytoskeleton & Actin Phalloidin @TRITC 532 (1:500) (red colour) represents the cytoskeleton/actin.

Figures 5.9A and B demonstrated the MSCs adhesion and proliferation after two time points. The greater cell adhesion at the TCP disk is attributed to the higher surface area of these samples. MSCs had the ability to adhere around the surface of the scaffolds as shown on the images and also showing a similar morphology to the cells grown on the control samples. A carpet-like cell layer covered all the samples at 2 and 4 days and this could be due to the cell number of the experiment (100000 cells/sample). The main MSC cell morphology included

cells that are flattened and enlarged. The focal adhesion points (vinculin antibody) were depended to the flattened morphology via dot like vinculin spots indicating mature FA for the 2 days and 4 days TCP sample and the 3D PCL scaffolds at 4 days. The more mature FAs showed increased cell spreading. At 2 days, the MSCs adhered on the 3D PCL scaffold included both dot and dash-like focal adhesion spots exhibiting less mature FAs due to the non-flattened cellular morphology. Figure 5.9B presented mainly a dash-like focal adhesion profile for the MSCs adhered on the 4D PCL/10%CA scaffolds demonstrating less mature FA points for the 2 days, while the TCP disk appeared to have similar observations to the other TCP disks, where the dot-like FA spots dominate.

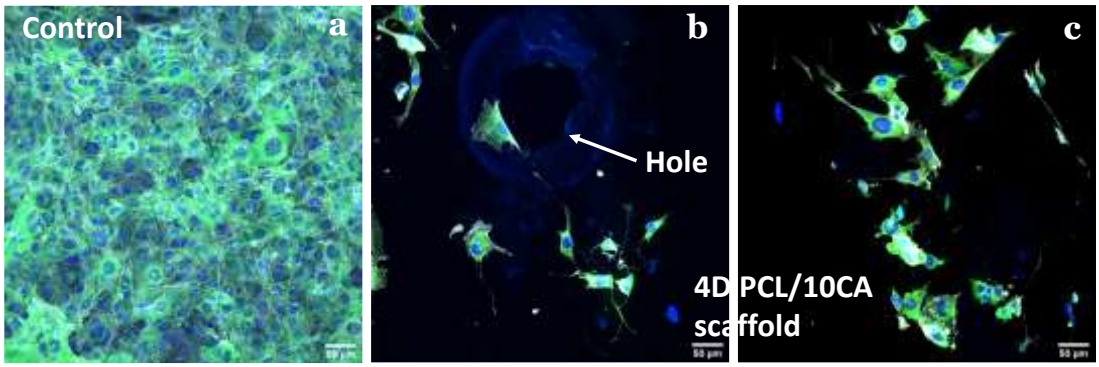

Figure 5.9B: Confocal images of Tissue Culture Plastic (TCP) disks (control) (a), and 4D PCL/10%CA scaffolds (b,c) cultured with MSCs for 2 days. In blue colour is the DAPI, representing the MSCs nucleus, Vin 488 (1:500, 1st and 2nd antibody) (green colour) represents the focal adhesion points on the cytoskeleton & Actin Phalloidin 568 (1:800) (grey colour) represents the cytoskeleton/actin.

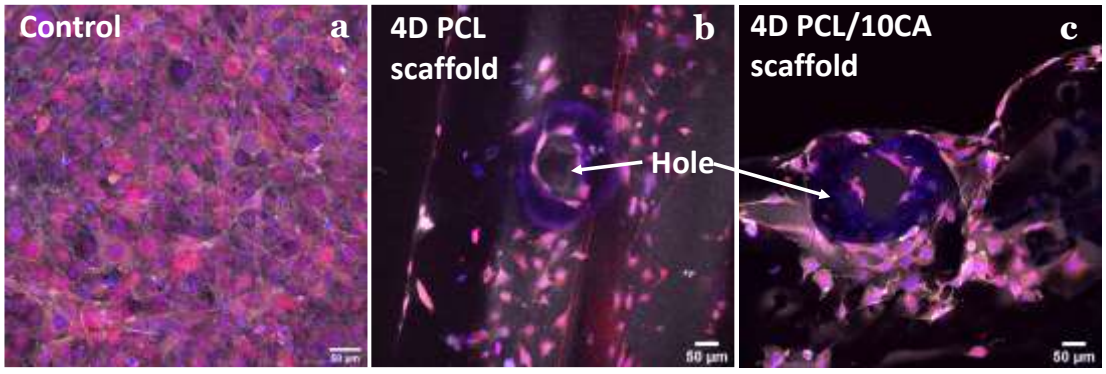

Figure 5.10: Confocal images of Tissue Culture Plastic (TCP) disks (control) (a), and 4D PCL (b) and 4D PCL/CA (c) scaffolds cultured with MSCs for 2 days. In blue colour is the DAPI, representing the MSCs nucleus, TAZ 647 (1:500, 1st and 2nd antibody) (red colour) plays a mechanotransductive role and it can be localized either in nucleus, or cytoplasm, or both, & Actin Phalloidin 568 (1:800) (grey colour) represents the cytoskeleton/actin.

It is observed that the cells adhered on the surfaces and they grew also in the holes. In addition, more nuclear TAZ localization was observed at the 4D PCL/10Ca scaffolds compared to the PCL scaffolds at 2 days indicating that the composite scaffold due to its different roughness and stiffness promotes the ability of MSCs cells to differentiate to osteogenic lineage(figure 5.11A and B). Moreover, the TCP disks demonstrated TAZ localization mainly on the nucleus for the 2 days in culture, while at 4 days there was cytoskeleton TAZ localization apparent too (Figure 5.11B).

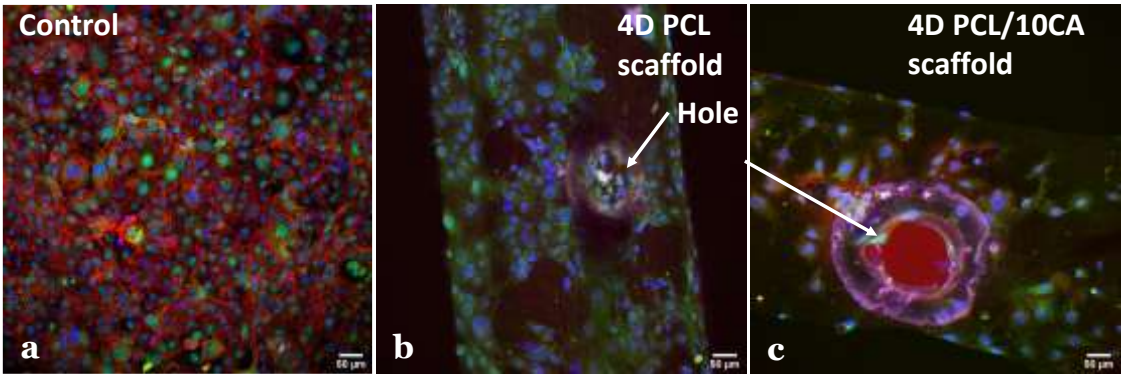

Figure 5.11A: Confocal images of Tissue Culture Plastic (TCP) disks (control) (a), and 4D PCL (b) and 4D PCL/CA (c) scaffolds cultured with MSCs for 2 days. In blue colour is the DAPI, representing the MSCs nucleus, TAZ 647 (1:500, 1st and 2nd antibody) (green colour) plays a mechanotransductive role and it can be localized either in nucleus, or cytoplasm, or both, & Actin Phalloidin 568 (1:800) (red colour) represents the cytoskeleton/actin.

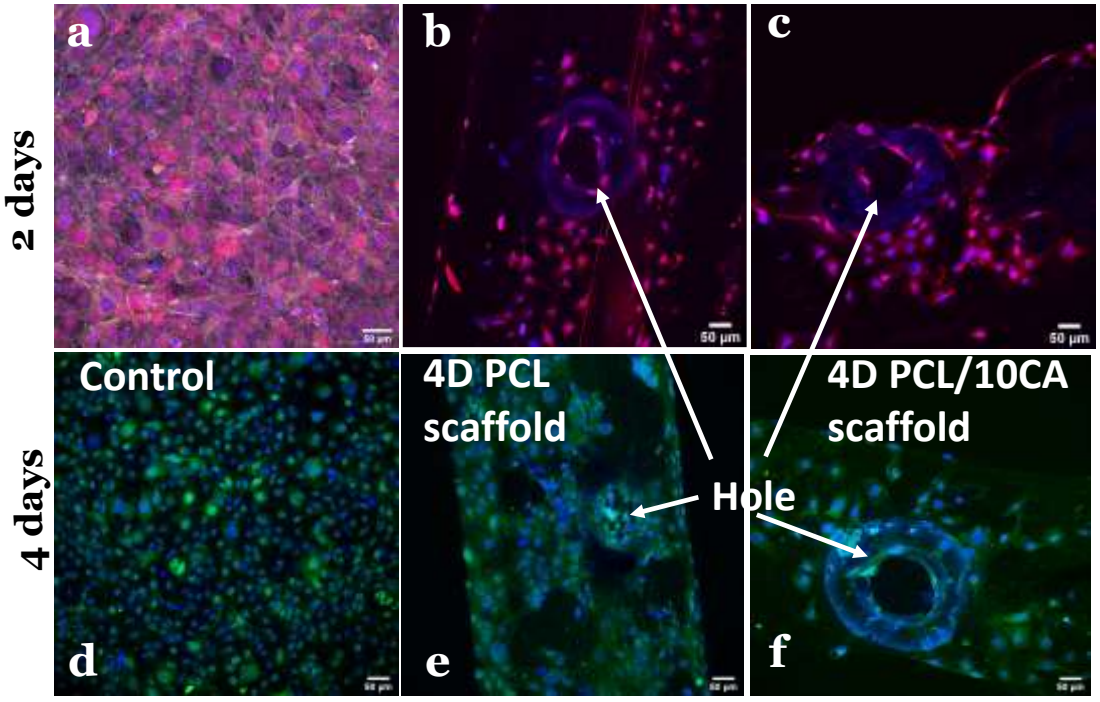

Figure 5.11B: Confocal images of Tissue Culture Plastic (TCP) disks (control) (a), and 4D PCL (b) and 4D PCL/CA (c) scaffolds cultured with MSCs for 2 days. In blue colour is the DAPI, representing the MSCs nucleus, TAZ 647 (1:500, 1st and

2nd antibody) (green colour) plays a mechanotransductive role and it can be localized either in nucleus, or cytoplasm, or both, & Actin Phalloidin 568 (1:800) (red colour) represents the cytoskeleton/actin.

These findings were obtained from two sets of experiments with 2-3 samples per group and comprise a preliminary study to investigate the effect of the printed scaffolds on cells. In order to be considered for their statistical significance, a series of extra experiments should be performed together with quantification of the confocal images eg. for TAZ localization. Furthermore mechanical measurements to determine the stiffness of the materials should be also considered.

Such 4D printed scaffolds with controlled micro and macro-porosities could be advanced and safer solutions for treating tissue defects eg bone without additional agents.

Conclusions

To conclude this thesis, several designs and parameters were tested in order to measure the power and limitations of our system and technique. Our aim was to combine 3d printing and laser ablation to create a novel system to create complex structures. As mentioned earlier, the hybrid system is able to offer more than 10 times better spatial resolution than a 3d printer device, due to the laser source. The fabrication of 4D PLA scaffolds with specific porosity, the characterization of the morphology, structure and wetting of these scaffolds, and the investigation of the behavior of various cells sum the research goals. This research did not come without any limitations. Several problems appeared on the CAD and 3d printing software. Most importantly, the mechanical movement and the physics of the 3d printer limit our capabilities. After several parameter adjustments, numerous scaffolds were printed and ablated layer by layer. The system and technique showed promising results in all the aspects of the state-of-the-art techniques too. Hierarchical structures were created, that among others, induce better osteogenesis. The micro-channels demonstrated in all three space dimensions could tackle the nutrient deficiency problem of modern techniques. Last but not least, the system is able to operate with composites, which are an important factor of material properties control.

More specifically, our results indicate that the 4D PLA scaffolds were successful as vessels for the various cell lines used (NIH 3T3, SW10, MSC), as they appear to adhere and proliferate on the 3d printed materials as well as inside the 4d hole structures. In order for best results, a manipulation of the laser ablation parameters is needed for each material and for the various cell lines. Similar results were derived from our study on 4D PCL scaffolds. The PCL material was easier to ablate than the PLA in the parameters used, probably due to its optical properties. Further investigation is needed to support this evidence. As a further step we investigated if different composite scaffolds could optimize the abovementioned results. The extruded PCL-CA10% filament was harder to print, due to the different heat properties of PCL and CA but the biological study showed similar results to the gold standard PLA and PCL materials. Different materials offer different mechanical, optical and other properties

Lastly, numerous scientific papers have shown that a big problem on tissue engineering is the shortage of oxygen and nutrients transferred on the harmed area. 4d scaffolds with micro-channels that resemble the body's vascularized system could tackle this problem, thus 4d PLA scaffolds with micro-channels were created to study microfluidics. The first results are promising concerning the possibilities of the system for microfluidics and is a logical step towards the next chapter of the project.

References

[1] Z. Jiao, B. Luo, S. Xiang, H. Ma, Y. Yu, and W. Yang, “3D printing of HA / PCL composite tissue engineering scaffolds,” *Advanced Industrial and Engineering Polymer Research*, vol. 2, no. 4, pp. 196–202, Oct. 2019, doi: 10.1016/j.aiepr.2019.09.003.

[2] A. Zaszczyńska, M. Moczulska-Heljak, A. Gradys, and P. Sajkiewicz, “Advances in 3D printing for tissue engineering,” *Materials*, vol. 14, no. 12. MDPI AG, Jun. 02, 2021. doi: 10.3390/ma14123149.

[3] X. Du, S. Fu, and Y. Zhu, “3D printing of ceramic-based scaffolds for bone tissue engineering: An overview,” *Journal of Materials Chemistry B*, vol. 6, no. 27. Royal Society of Chemistry, pp. 4397–4412, 2018. doi: 10.1039/c8tb00677f.

[4] J. bin Lee, W. Y. Maeng, Y. H. Koh, and H. E. Kim, “Porous calcium phosphate ceramic scaffolds with tailored pore orientations and mechanical properties using lithography-based ceramic 3D printing technique,” *Materials*, vol. 11, no. 9, Sep. 2018, doi: 10.3390/ma11091711.

[5] U. Jammalamadaka and K. Tappa, “Recent advances in biomaterials for 3D printing and tissue engineering,” *Journal of Functional Biomaterials*, vol. 9, no. 1. MDPI AG, Mar. 01, 2018. doi: 10.3390/jfb9010022.

[6] L. Papadimitriou, P. Manganas, A. Ranella, and E. Stratakis, “Biofabrication for neural tissue engineering applications,” *Materials Today Bio*, vol. 6. Elsevier B.V., Mar. 01, 2020. doi: 10.1016/j.mtbio.2020.100043.

[7] M. Malinauskas *et al.*, “3D microporous scaffolds manufactured via combination of fused filament fabrication and direct laser writing ablation,” *Micromachines (Basel)*, vol. 5, no. 4, pp. 839–858, 2014, doi: 10.3390/mi5040839.

[8] N. E. Fedorovich *et al.*, “Biofabrication of osteochondral tissue equivalents by printing topologically defined, cell-laden hydrogel scaffolds,” *Tissue Eng Part C Methods*, vol. 18, no. 1, pp. 33–44, Jan. 2012, doi: 10.1089/ten.tec.2011.0060.

[9] I. A. Otto *et al.*, “Biofabrication of a shape-stable auricular structure for the reconstruction of ear deformities,” *Mater Today Bio*, vol. 9, Jan. 2021, doi: 10.1016/j.mtbio.2021.100094.

[10] M. S. Mannoor *et al.*, “3D Printed Bionic Ears,” *Nano Lett*, vol. 13, no. 6, pp. 2634–2639, Jun. 2013, doi: 10.1021/nl4007744.

[11] N. A. Kurniawan, “The ins and outs of engineering functional tissues and organs: Evaluating the in-vitro and in-situ processes,” *Current Opinion in Organ Transplantation*, vol. 24, no. 5. Lippincott Williams and Wilkins, pp. 590–597, Oct. 01, 2019. doi: 10.1097/MOT.0000000000000690.

[12] S. Mohaghegh, S. F. Hosseini, M. R. Rad, and A. Khojateh, “3D Printed Composite Scaffolds in Bone Tissue Engineering: A systematic review,” *Curr Stem Cell Res Ther*, vol. 16, Sep. 2021, doi: 10.2174/1574888x16666210810111754.

[13] L. Roseti *et al.*, “Scaffolds for Bone Tissue Engineering: State of the art and new perspectives,” *Materials Science and Engineering C*, vol. 78. Elsevier Ltd, pp. 1246–1262, Sep. 01, 2017. doi: 10.1016/j.msec.2017.05.017.

[14] D. H. Rosenzweig, E. Carelli, T. Steffen, P. Jarzem, and L. Haglund, “3D-printed ABS and PLA scaffolds for cartilage and nucleus pulposustissue regeneration,” *Int J Mol Sci*, vol. 16, no. 7, pp. 15118–15135, Jul. 2015, doi: 10.3390/ijms160715118.

[15] M. Mohseni, D. W. Hutmacher, and N. J. Castro, “Independent evaluation of medical-grade bioresorbable filaments for fused deposition modelling/fused filament fabrication of tissue engineered constructs,” *Polymers (Basel)*, vol. 10, no. 1, Jan. 2018, doi: 10.3390/polym10010040.

[16] J.-Y. Rho, L. Kuhn-Spearing, and P. Zioupos, “Mechanical properties and the hierarchical structure of bone,” 1998.

[17] M. Eryildiz, “Investigation of Mechanical and Biological Properties of FDM 3D-Printed PLA Scaffolds With Radial Gradient Porosity for Tissue Engineering,” 2021, doi: 10.21203/rs.3.rs-944744/v1.

[18] S. Bose, S. Vahabzadeh, and A. Bandyopadhyay, “Bone tissue engineering using 3D printing,” *Materials Today*, vol. 16, no. 12. pp. 496–504, Dec. 2013. doi: 10.1016/j.mattod.2013.11.017.

[19] A. Haleem, M. Javaid, R. H. Khan, and R. Suman, “3D printing applications in bone tissue engineering,” *J Clin Orthop Trauma*, vol. 11, pp. S118–S124, Feb. 2020, doi: 10.1016/j.jcot.2019.12.002.

[20] A. Haleem, M. Javaid, R. H. Khan, and R. Suman, “3D printing applications in bone tissue engineering,” *J Clin Orthop Trauma*, vol. 11, pp. S118–S124, Feb. 2020, doi: 10.1016/j.jcot.2019.12.002.

[21] R. Dwivedi *et al.*, “Polycaprolactone as biomaterial for bone scaffolds: Review of literature,” *Journal of Oral Biology and Craniofacial Research*, vol. 10, no. 1. Elsevier B.V., pp. 381–388, Jan. 01, 2020. doi: 10.1016/j.jobcr.2019.10.003.

[22] A. D. Bagde *et al.*, “State of the Art Technology for Bone Tissue Engineering and Drug Delivery,” *IRBM*, vol. 40, no. 3. Elsevier Masson SAS, pp. 133–144, Jun. 01, 2019. doi: 10.1016/j.irbm.2019.03.001.

[23] X. Li *et al.*, “3D printing of hydroxyapatite/tricalcium phosphate scaffold with hierarchical porous structure for bone regeneration,” *Biodes Manuf*, vol. 3, no. 1, pp. 15–29, Mar. 2020, doi: 10.1007/s42242-019-00056-5.

[24] V. Guduric, “3D Printing and Characterization of PLA Scaffolds for Layer-by-Layer BioAssembly in Tissue Engineering.” [Online]. Available: https://tel.archives-ouvertes.fr/tel-01865824

[25] A. Dey, I. N. R. Eagle, and N. Yodo, “A review on filament materials for fused filament fabrication,” *Journal of Manufacturing and Materials Processing*, vol. 5, no. 3. MDPI AG, Sep. 01, 2021. doi: 10.3390/jmmp5030069.

[26] G. H. Wu and S. H. Hsu, “Review: Polymeric-based 3D printing for tissue engineering,” *J Med Biol Eng*, vol. 35, no. 3, pp. 285–292, Jun. 2015, doi: 10.1007/s40846-015-0038-3.

[27] M. Terakawa, “Femtosecond Laser Processing of Biodegradable Polymers,” *Applied Sciences*, vol. 8, no. 7, p. 1123, Jul. 2018, doi: 10.3390/app8071123.

[28] C. A. Murphy, J. B. Costa, J. Silva-Correia, J. M. Oliveira, R. L. Reis, and M. N. Collins, “Biopolymers and polymers in the search of alternative treatments for meniscal regeneration: State of the art and future trends,” *Applied Materials Today*, vol. 12. Elsevier Ltd, pp. 51–71, Sep. 01, 2018. doi: 10.1016/j.apmt.2018.04.002.

[29] D. Singh, D. Singh, and S. S. Han, “3D printing of scaffold for cells delivery: Advances in skin tissue engineering,” *Polymers*, vol. 8, no. 1. MDPI AG, 2016. doi: 10.3390/polym8010019.

[30] D. Veeman *et al.*, “Additive Manufacturing of Biopolymers for Tissue Engineering and Regenerative Medicine: An Overview, Potential Applications, Advancements, and Trends,” *International Journal of Polymer Science*, vol. 2021. Hindawi Limited, 2021. doi: 10.1155/2021/4907027.

[31] R. Ortiz, I. Aurrekoetxea-Rodríguez, M. Rommel, I. Quintana, M. Vivanco, and J. Toca-Herrera, “Laser Surface Microstructuring of a Bio-Resorbable Polymer to Anchor Stem Cells, Control Adipocyte Morphology, and Promote Osteogenesis,” *Polymers (Basel)*, vol. 10, no. 12, p. 1337, Dec. 2018, doi: 10.3390/polym10121337.

[32] J. Babilotte *et al.*, “Development and characterization of a PLGA-HA composite material to fabricate 3D-printed scaffolds for bone tissue engineering,” *Materials Science and Engineering C*, vol. 118, Jan. 2021, doi: 10.1016/j.msec.2020.111334.

[33] N. Siddiqui, S. Asawa, B. Birru, R. Baadhe, and S. Rao, “PCL-Based Composite Scaffold Matrices for Tissue Engineering Applications,” *Molecular Biotechnology*, vol. 60, no. 7. Humana Press Inc., pp. 506–532, Jul. 01, 2018. doi: 10.1007/s12033-018-0084-5.

[34] N. Rodrigues, M. Benning, A. M. Ferreira, L. Dixon, and K. Dalgarno, “Manufacture and Characterisation of Porous PLA Scaffolds,” in *Procedia CIRP*, 2016, vol. 49, pp. 33–38. doi: 10.1016/j.procir.2015.07.025.

[35] “https://www.protolabs.com/resources/blog/types-of-3d-printing/.”

[36] E. Stratakis, “Additive Manufacturing-AM (3D and 4D printing).”

[37] “Subtractive Manufacturing and Conventional Biofabrication Approaches.”

[38] “https://www.explainthatstuff.com/how-3d-printers-work.html.”

[39] “https://patents.google.com/patent/US5121329”

[40] “https://www.aniwaa.com/resource/am-materials/peek-3d-printing-how-to-prevent-warping/.”

[41] “https://www.hubs.com/knowledge-base/what-is-fdm-3d-printing/.”

[42] “https://en.wikipedia.org/wiki/Polylactic_acid.”

[43] “polycaprolactone PCL.”

[44] C. Gauss, K. L. Pickering, and L. P. Muthe, “The use of cellulose in bio-derived formulations for 3D/4D printing: A review,” *Composites Part C: Open Access*, vol. 4. Elsevier B.V., Mar. 01, 2021. doi: 10.1016/j.jcomc.2021.100113.

[45] “https://en.wikipedia.org/wiki/Gaussian_beam.”

[46] G. Nicolodelli, R. de Fátima Zanirato Lizarelli, and V. Salvador Bagnato, “Influence of effective number of pulses on the morphological structure of teeth and bovine femur after femtosecond laser ablation,” *J Biomed Opt*, vol. 17, no. 4, p. 048001, 2012, doi: 10.1117/1.jbo.17.4.048001.

[47] J. Krüger and W. Kautek, “Ultrashort Pulse Laser Interaction with Dielectrics and Polymers,” in *Advances in Polymer Science*, vol. 168, 2004, pp. 247–290. doi: 10.1007/b12683.

[48] A. H. Hamad, “Effects of Different Laser Pulse Regimes (Nanosecond, Picosecond and Femtosecond) on the Ablation of Materials for Production of Nanoparticles in Liquid Solution,” in *High Energy and Short Pulse Lasers*, InTech, 2016. doi: 10.5772/63892.

[49] C. B. Schaffer, A. Brodeur, and E. Mazur, “Laser-induced breakdown and damage in bulk transparent materials induced by tightly focused femtosecond laser pulses,” *Meas Sci Technol*, vol. 12, no. 11, pp. 1784–1794, 2001, doi: 10.1088/0957-0233/12/11/305.

[50] E. Stratakis and V. Zorba, “Biomimetic Artificial Nanostructured Surfaces,” 2012. doi: 10.1002/9783527610419.ntls0213.

[51] E. Stratakis *et al.*, “Laser engineering of biomimetic surfaces,” *Materials Science and Engineering: R: Reports*, vol. 141, p. 100562, 2020, doi: https://doi.org/10.1016/j.mser.2020.100562.

[52] D. Bäuerle, “Laser Processing and Chemistry Fourth Edition,” 2011.

[53] “https://en.wikipedia.org/wiki/Scanning_electron_microscope.”

[54] Manoudis P., “Study and evaluation of protective coatings for the surgace protection and conservation of monuments of cultural heritage.”

[55] “https://www.leica-microsystems.com/science-lab/brief-introduction-to-coating-technology-for-electron-microscopy/.”

[56] “https://en.wikipedia.org/wiki/Sputter_deposition.”

[57] “confocal microscopy”.

[58] “PMC4379090”.

[59] X. Guan *et al.*, “Development of hydrogels for regenerative engineering,” *Biotechnol J*, vol. 12, no. 5, p. 1600394, May 2017, doi: 10.1002/biot.201600394.

[60] M. J. Kraeutler, J. W. Belk, J. M. Purcell, and E. C. McCarty, “Microfracture Versus Autologous Chondrocyte Implantation for Articular Cartilage Lesions in the Knee: A Systematic Review of 5-Year Outcomes,” *Am J Sports Med*, vol. 46, no. 4, pp. 995–999, Mar. 2018, doi: 10.1177/0363546517701912.

[61] A. G. Guex *et al.*, “Fine-tuning of substrate architecture and surface chemistry promotes muscle tissue development,” *Acta Biomater*, vol. 8, no. 4, pp. 1481–1489, Apr. 2012, doi: 10.1016/j.actbio.2011.12.033.

[62] E. Bogdan and P. Michorczyk, “3d printing in heterogeneous catalysis—the state of the art,” *Materials*, vol. 13, no. 20. MDPI AG, pp. 1–23, Oct. 02, 2020. doi: 10.3390/ma13204534.

[63] S. Pina *et al.*, “Biofunctional Ionic-Doped Calcium Phosphates: Silk Fibroin Composites for Bone Tissue Engineering Scaffolding,” *Cells Tissues Organs*, vol. 204, no. 3–4, pp. 150–163, 2017, doi: 10.1159/000469703.

[64] J. Alves da Silva, A. Sarti, S. I. Maintinguer, I. M. Kaiser, and G. H. R. da Silva, “Performance of an anaerobic baffled reactor with an aerobic chamber treating low-strength wastewater,” *Desalination Water Treat*, vol. 100, pp. 1–10, 2017, doi: 10.5004/dwt.2017.21713.

[65] A. I. Gonçalves, M. T. Rodrigues, and M. E. Gomes, “Tissue-engineered magnetic cell sheet patches for advanced strategies in tendon regeneration,” *Acta Biomater*, vol. 63, pp. 110–122, Nov. 2017, doi: 10.1016/j.actbio.2017.09.014.

[66] P. Diloksumpan *et al.*, “Combining multi-scale 3D printing technologies to engineer reinforced hydrogel-ceramic interfaces,” *Biofabrication*, vol. 12, no. 2, 2020, doi: 10.1088/1758-5090/ab69d9.

[67] W. He, J. Wu, J. Xu, D. A. Mosselhy, Y. Zheng, and S. Yang, “Bacterial Cellulose: Functional Modification and Wound Healing Applications,” *Adv Wound Care (New Rochelle)*, vol. 10, no. 11, pp. 623–640, Sep. 2020, doi: 10.1089/wound.2020.1219.

[68] H. El-Hamshary, M. E. El-Naggar, A. El-Faham, M. A. Abu-Saied, M. K. Ahmed, and M. Al-Sahly, “Preparation and Characterization of Nanofibrous Scaffolds of Ag/Vanadate Hydroxyapatite Encapsulated into Polycaprolactone: Morphology, Mechanical, and In Vitro Cells Adhesion,” *Polymers (Basel)*, vol. 13, no. 8, 2021, doi: 10.3390/polym13081327.

[69] X. Li *et al.*, “3D printing of hydroxyapatite/tricalcium phosphate scaffold with hierarchical porous structure for bone regeneration,” *Biodes Manuf*, vol. 3, no. 1, pp. 15–29, 2020, doi: 10.1007/s42242-019-00056-5.

[70] J. Babilotte *et al.*, “Development and characterization of a PLGA-HA composite material to fabricate 3D-printed scaffolds for bone tissue engineering,” *Materials Science and Engineering: C*, vol. 118, p. 111334, 2021, doi: https://doi.org/10.1016/j.msec.2020.111334.

[71] “13985244”.

APPENDIX A

A.1 Warping

Warping is a common defect in 3D printers, caused by poor temperature control. When the material exits the nozzle, it exists in liquid form with high temperature (T_H). During solidification, the dimensions of the material decrease until it reaches room temperature (T_c). Not all dimensions decrease homogenously, though. The hot layer follows an exponential decrease, but the lower layer has its temperate risen in the beginning, when it comes in contact with the hot layer, before it decreases back to room temperature. This causes internal stress, that tries to pull the layers upwards.

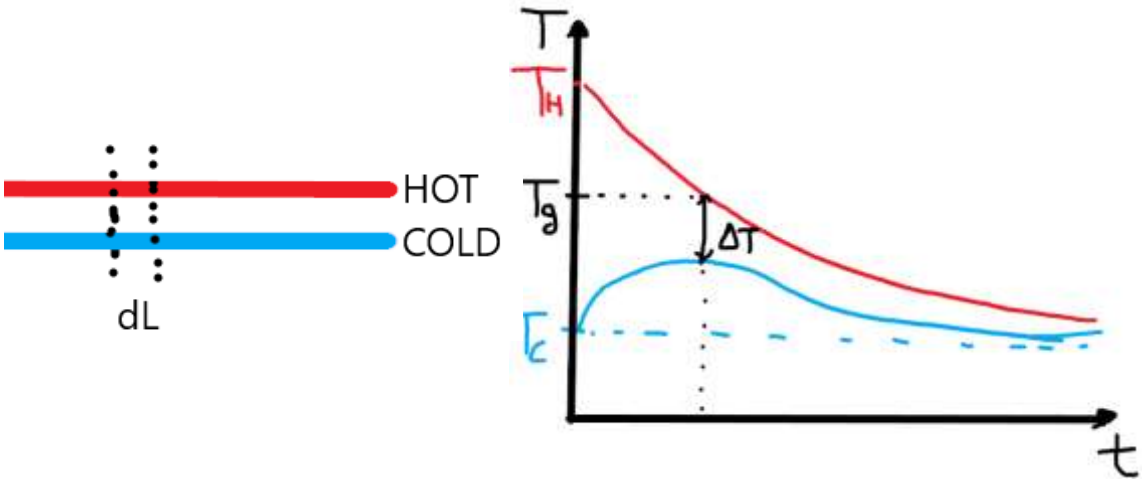

Fig. A.1. Warping physics explanation. Warping is a result of the thermal difference between the cold environment and the hot liquid material.

Thermal expansion difference formula explains the warping:

$$\Delta L/L = c * \Delta T \qquad (A.1)$$

As seen on fig. A.1, the already extruded material has reached room temperature, while the next layer of material exiting the nozzle has a much higher temperature. This high temperature difference causes contraction of the material that is noticeable below its glass transition temperature (T_g), because that's where it solidifies.

A.2 Layer adhesion

Layer adhesion is critical for making a high end 3d-printed object. When material exits the nozzle, it has liquid form due to the high temperature and pressure. The layers bond to each other while solidifying under room temperature.

Layers bond strength is always lower than the base strength of the material. This leads to printed parts that have more strength in the XY plane that in the Z. The theoretical extrusion profile is spherical, but because each extruded layer is pressed against the previously printed layer, the real extrusion profile of the material is an oval (fig. A.2) [41].

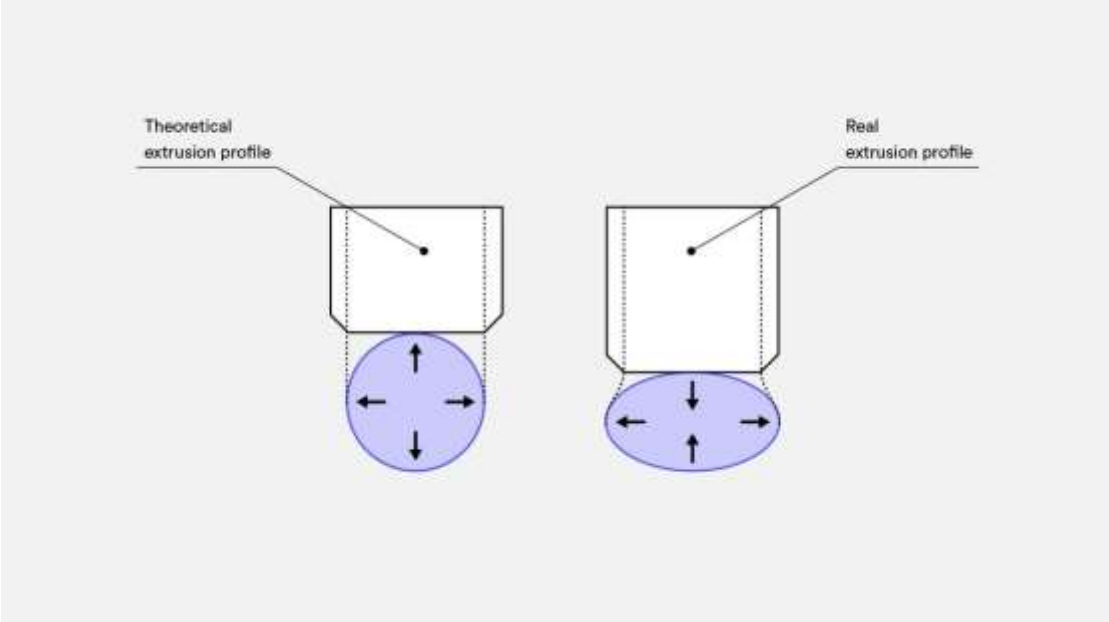

Fig. A.2. The FDM material extrusion profile [41].